Energy Conversion and Management 324 (2025) 119260

Contents lists available at ScienceDirect

Energy Conversion and Management

journal homepage: www.elsevier.com/locate/enconman

Research Paper

A study on the combination of crystallization-controllable phase change materials and solar-assisted heat pump for electricity demand shifting in space heating

Cagri Kutlu [a,*], Mehmet Tahir Erdinc [a,b], Abdullah Dik [a], Ziwei Chen [a], Qinghua Lyu [c], Yuehong Su [a], Saffa Riffat [a]

[a] Department of Architecture and Built Environment, University of Nottingham, University Park NG7 2RD, UK
[b] Department of Mechanical Engineering, Tarsus University, 33400 Tarsus/Mersin, Turkey
[c] School of Science, Hubei University of Technology, Hubei, Wuhan, China

ARTICLE INFO

Keywords:
Space heating
Electricity demand shifting
Crystallization-controllable phase change materials (PCM)
Supercooled PCM
Sodium Acetate Trihydrate (SAT)
Crystallization triggering
Solar-assisted heat pump

ABSTRACT

Supercooled phase change materials offer a promising solution for space heating due to their ability to release latent heat upon crystallization initiation, even when stored at ambient temperatures. This unique property makes them ideal for solar-assisted space heating, where external activation enables on-demand heat release, addressing the critical need for energy-efficient heating solutions. In this study, a system promoting demand shifting is proposed, aiming to transfer energy consumption from morning and evening peak periods to daytime and high solar irradiance days, thereby enhancing the efficiency of solar heat pumps and reducing grid stress through the use of supercooled crystallization-controllable phase change materials. A model was developed, consisting of evacuated tube collectors, a buffer tank, heat storage tanks with crystallization-controllable phase change material, and a building heating demand model. The study introduces a novel system control methodology, focusing on an effective operation of tank shifting based on the heating requirement and solar energy availability. Real weather data were used to calculate system performance. With 50 m^2 of collectors, a 1000-liter buffer tank, and a heat pump with a maximum output of 7 kW, the heat storage tanks are charged and discharged following the developed operational methodology. The system achieved a weekly coefficient of performance of 3.56 and successfully shifted electricity demand to solar hours, with only 28.5% of the total consumption occurring during domestic morning and evening peak times.

1. Introduction

The integration of thermal energy storage into heating systems offers an efficient means to harness renewable energy sources within the building energy infrastructure [1]. This integration not only reduces greenhouse gas emissions but also enhances the overall sustainability of these systems. Moreover, thermal energy storage technology is one of the solutions for grid flexibility and renewable energy utilization, by reducing electricity consumption during peak times and balancing the grid fluctuations [2]. Among the various thermal energy storage materials available, this study focuses on latent heat storage using phase change materials (PCM). PCMs have gained popularity in both research and commercial markets due to their high energy density and the capability to store and release heat within a narrow temperature range [3]. Numerous studies have been conducted to explore the impact of integrating latent heat storage on domestic hot water (DHW) and space heating applications [4].

Among latent heat storage materials, sodium acetate trihydrate (SAT) is distinguished by its numerous benefits, including high latent heat capacity, non-toxicity, and cost-effectiveness. The melting point of SAT at 58 °C makes it exceptionally suitable for space heating systems and providing domestic hot water to end-users. However, similar to other salt hydrate PCMs, SAT presents certain challenges, such as low thermal conductivity, a tendency for supercooling, the possibility of phase separation, and a risk of corrosion when in contact with common heat exchanger materials [5]. Several attempts have been made to address these challenges, including efforts to increase thermal conductivity [6], stabilize supercooling [7], and eliminate phase separation [8],

---

* Corresponding author.
E-mail address: cagri.kutlu2@nottingham.ac.uk (C. Kutlu).

https://doi.org/10.1016/j.enconman.2024.119260
Received 25 May 2024; Received in revised form 1 October 2024; Accepted 8 November 2024

by introducing various materials and agents. Despite these challenges, SAT's notable property of significant supercooling holds promise for thermal storage applications. Its latent heat is only released upon triggering crystallization, even when stored at ambient temperatures for extended periods [9].

To enhance the stability of supercooling, various strategies have been explored. Dannemand et al. [10] suggested that charging SAT at higher temperatures, specifically between 84 °C and 94 °C, enhances the stability of supercooling based on their comprehensive experiments. However, in this study, a charging temperature of 70 °C is used to explore the feasibility of achieving stable supercooling with lower energy input by ensuring that all PCM crystals are fully melted in simulations. This approach aligns with efforts to optimize energy use in practical applications. When stable supercooling and controllable crystallization are achieved, this distinctive characteristic facilitates the integration of PCM systems with intermittent renewable energy sources, such as solar thermal collectors and heat pump units. [11]. In the context of enhancing energy flexibility and enabling decarbonization through heat pump technology, SAT holds particular relevance. Integrating SAT with heat pump systems could significantly advance their efficiency and thermal storage capabilities in short term to mid-term. The ability of SAT to store heat in its latent form and release it on demand complements the operation of heat pumps, which are often challenged by variable output depending on external temperatures and energy demand fluctuations. Moreover, integration of SAT into the heat pump system aligns with the shift towards renewable energy sources by smoothing out the variability in energy production and consumption therefore, it becomes crucial for developing next-generation energy systems that are both sustainable and capable of supporting large-scale decarbonization efforts.

The key to harnessing this feature of controllable crystallization lies in the trigger mechanism, which controls the timing of the crystallization of sodium acetate from its supercooled state, thereby releasing the stored heat energy. Various techniques have been explored to trigger the release of latent heat from supercooled SAT. Electrical triggering, in particular, shows promise due to the advantages of using a compact device, enabling system automation, and requiring only a minimal amount of power [12]. The use of silver electrodes for examining electrical nucleation was advanced by Sakuraki et al. [12], aiming to refine the specifications of Ag electrodes and voltage control conditions for stable triggering performance. Dong et al. [13] conducted experimental investigations on electrical triggering using different electrode materials, electrode diameters and applied voltages to initiate the nucleation of SAT. Subsequently, they developed composites combining SAT with copper foam and expanded graphite to enhance thermal conductivity, achieving electrically-triggered crystallization of these composite PCMs [14]. Utilizing local cooling through the Peltier effect is another potential method for automating the triggering process which was successfully applied in experiments [15].

The potential of using controllable crystallisation of the SAT was demonstrated by studies. For direct charging by solar collectors, Dannemand et al. [16] carried out TRNSYS simulation after experimentally improving the SAT storage drawbacks, such as phase separation and unstable supercooling. They concluded that by employing 36 m^2 solar collectors, 80% solar fraction can be achievable using 7 modules of 150 L SAT for a Danish Passive house. Englmair et al. [17] conducted a numerical study demonstrating that a solar combi-system incorporating on-demand crystallization of supercooled SAT composites can provide a promising 56% annual solar fraction of heat supply, particularly suitable for passive houses. Englmair et al. [18] tested the triggering of the SAT storage unit using a developed mechanical seed crystal injection device, reporting that 80% of the fusion heat was effectively discharged. Kutlu et al. [19] conducted a simulation study on a solar-assisted heat pump unit with a 4 m^2 collector area, equipped with a PCM-immersed water tank. Their results showed that the controlled crystallization of SAT can reduce the daily energy consumption for DHW by approximately 13% on an average solar day. Furthermore, Kutlu et al. [20] utilized a crystallization-controlled supercooled PCM in a direct-expansion solar-assisted heat pump unit to provide space heating and DHW. By developing a methodology for controlling heat pump operation, they found that the overall COP for one month of operation was 3.98. Zhou et al. [21] conducted experiments with a rounded rectangular SAT storage unit for room heating. They found that triggering the SAT unit effectively heats the room and maintains its temperature above the initial state. Kutlu et al. [22] advanced the control strategies and investigated the dynamic thermal behaviour of a supercooled PCM-immersed storage tank, focusing on the effects of different PCM tube activation sequences. Their findings suggest that controlling the activation order of PCM tubes can increase the hot water supply temperature compared to activating all tubes simultaneously at midnight. This strategy improved heating performance across various UK heating profiles, resulting in an average 1.5 °C increase in delivery temperature under the same conditions. Lastly, Chen et al. [23] carried out a modelling study to explore the impact of utilizing supercooled salt hydrate units, including SAT, for controlled heat release in greenhouses. They employed seasonally stored latent heat in these units to provide heating when daily storage was insufficient to maintain the required indoor temperature. Their findings indicate that supercooled PCMs can provide 2–5 h of heating, sufficient to maintain the desired indoor temperature.

1.1. Load shifting and flexibility

Using thermal storage in heat pump systems is essential for shifting the load on the grid and operating the system using demand-side management methods. Although there are various control strategies aimed at achieving goals such as low operational costs, maximum thermal comfort, and minimal carbon emissions, moving heating and cooling loads from off-peak to low-demand periods is also effective [24]. The integration of smart grids and heat pumps in literature focuses on three main objectives: grid ancillary services, financial sustainability, and renewable energy integration [25]. There is extensive literature detailing the parameters and strategies in these areas, as found in reference [25]. Kelly et al.[26] conducted a simulation study on an air source heat pump equipped with thermal storage to shift the load to off-peak periods for electricity network operators in a typical UK detached dwelling. The off-peak periods were identified as from midnight to 5 AM, 1 PM to 4 PM, and 8 PM to 10 PM, during which the heat pump operates and charges the buffer tank. However, they discovered that the average COP of the heat pump with load shifting is lower than that of the heat pump without any storage, due to heat loss from the storage and nighttime operation. Baeten et al. [27] presented a multi-objective model predictive control strategy for a system comprising a heat pump and thermal energy storage in a residential demand response context. The analysis took into account users' energy costs, the environmental impact of energy use, and the impact of expanding electricity generation capacity. They concluded that strategic adjustments and additional storage can reduce peak load capacity to pre-heat pump levels and decrease reliance on peak power plants by up to 11%, though these benefits come at the cost of higher operational expenses for consumers. It should be noted that the investigated system includes PV and wind power generation, and the proposed control strategy optimizes operation by considering these renewable energy sources. Le et al. [24] investigated three load-shifting strategies for a cascade heat pump unit under Northern Ireland's weather conditions. These strategies included utilizing a low-price electricity tariff, operating the unit during daytime to benefit from higher outdoor temperature and higher COPs, and a hybrid strategy that combines the advantages of nighttime cheaper electricity rates and daytime higher ambient temperatures. They concluded that the hybrid strategy is the most effective. In this strategy, the cascade heat pump is programmed to charge the thermal energy storage at 3 AM, taking advantage of low electricity rates, and at 2 PM, benefiting from high ambient temperatures, followed by discharging in the morning and afternoon.

It can be noted that strategies focused on grid load, electricity pricing, or periods for integrating renewable energy may vary across different countries. Nevertheless, in the UK and many other developed nations, there is an intensive push to replace carbon-intensive gas boilers with efficient heat HPs. A report from the UK Parliament [28] reveals that 72,000 HP units were installed in the UK in 2022. This supports the UK government's ambitious goal to ramp up annual HP installations to 600,000 units by 2028. Given this objective, a substantial rise in the deployment of HPs in the UK is expected in the coming years. A study by Watson et al. [29] on the prediction of future heat pump electricity demand in Great Britain indicated that the widespread adoption of heat pumps will significantly increase overall electricity demand and alter the demand profile. This increase in HP penetration is likely to emphasize morning and evening peak demand patterns, underscoring the importance of load shifting. Additionally, recent research by Dik et al. [30] suggests that the UK distribution networks are currently inadequate to handle a scenario of 100% electric vehicle (EV) adoption without management strategies. The combined adoption of EVs and HPs is expected to place considerable strain on the grid. As a result, implementing effective load shifting strategies will be crucial to mitigate peak load challenges associated with HP operation. Thus, one of the aims of this study is to demonstrate how the integration of SAT can enhance operational flexibility and successfully shift the demand.

1.2. *Objectives of this study*

As given, implementing intelligent control methods for managing heat pumps connected to thermal storage can significantly enhance the efficiency of energy systems and helps to reduce grid stress. These methods boost flexibility, facilitating the shift towards a more sustainable, low-carbon electricity network while offering substantial economic and environmental advantages [31]. By addressing the challenges of intermittent energy and also considering factors such as the growing number of EVs and their additional stress on the grid, smart energy storage systems need to be developed to work with heat pumps [32]. These systems should be based on strategies that control and benefit from flexible operation by shifting the load.

Given the urgent need for decarbonization and enhanced energy flexibility, this research explores the integration of controllable crystallisation of SAT with heat pump systems, aiming to improve their flexibility and thermal storage capabilities significantly. This integration facilitates for making it crucial for developing next-generation energy systems that support large-scale decarbonization efforts. Thus, proposed approach utilizing electrical triggering mechanisms to control the timing of SAT crystallization from its supercooled state, potentially makes it promising in PCM applications in heat pump operations and enhancing their operational flexibility and efficiency.

In order to show operation capacity and performance of the proposed system, this study conducts a comparative analysis of three distinct systems: a traditional air source heat pump (ASHP), a conventional solar-assisted heat pump (SAHP), and an controllable-crystallization PCM integrated SAHP system. Based on the reference study [11], where SAT PCM tubes were submerged in water tanks, the proposed system explores the feasibility of PCM integration for enhanced thermal storage. Recognizing space constraints in new building designs, the proposed system design capitalizes on the minimal heat loss characteristics of PCM storage, enabling versatile placement options including underground or external installations without the risk of thermal degradation thanks to the supercooling feature. A novel system control methodology is introduced, focusing on a effective weekly storage tank shifting operation. This approach provides new insights into effectively transitioning energy demand from peak to off-peak periods, optimizing energy consumption and demonstrating the system's adaptability to dynamic energy markets.

2. Methods

The proposed system comprises evacuated tube solar collectors, a buffer tank, a heat pump unit, and SAT storage tanks situated underground. This design enables the utilization of multiple storage tanks, which can be charged during periods of high solar radiation and utilized later when solar energy is scarce or insufficient. The UK national electric load profile remains high during daytime due to office and industrial usage, making it potentially beneficial to shift heating loads to nighttime for now. However, as stated in recent papers, trends in heat pump usage and factors such as EV integration into the grid are expected to sharply increase electricity usage in the grid during morning and evening peak times. Furthermore, solar power contributed 4.9% to the UK's renewable energy mix in 2023, with projections suggesting that solar capacity could grow to roughly 70GW by 2030 [33]. Therefore, as the contribution of solar energy increases, it would be more advantageous to operate heat pump systems during the daytime for both low carbon supply and efficient operation.

The system's configuration is illustrated in Fig. 1, with the operations for charging and discharging explained as follows:

Charging period: When solar energy is available, the system operates in charging mode. As the system has a buffer tank, solar assisted heat pump can charge the SAT tanks any time in the day, however, in this concept, charging time is limited with the daytime period to contribute to demand shifting and to avoid low-efficiency operation of the heat pump due to the low temperature of the heat source. Solar collectors harvest the solar energy and store it in the buffer tank when the solar energy is available regardless of the intensity of the solar irradiance. The heat pump uses the stored heat inside the buffer tank as a heat source and boosts the temperature of the circulating water up to 70 °C in order to charge the SAT storage tank.

Discharging period: When heating is required by the building, heat transfer water is circulated between the building and the SAT storage unit. Activated supercooled PCMs increase the water temperature to 54–56 °C. Although these temperatures seem not as high as a usual boiler system's operation temperature, it can be assumed as a sufficient radiator area is provided in the house. Besides, Jangsten et al. [34] presented data from a survey and they concluded that the ambient temperature influences the hot water supply temperature such as the average supply temperature is 64 °C when the outdoor temperature is −16 °C and 55 °C when the outdoor temperature is 5 °C.

In order to highlight the system's advantages in energy saving, carbon emission reduction, and grid relief potential, both SAHP and ASHP are modelled. Their performances are then compared. Fig. 2 illustrates the integration of these two units into the building heating system. The performance of the ASHP system is directly influenced by ambient temperature. When the ambient temperature drops below 4 °C, especially with high relative humidity, a further performance decline occurs as defrosting becomes necessary for the outdoor unit. The operation of the SAHP unit is as follows: Solar collectors store solar energy in the

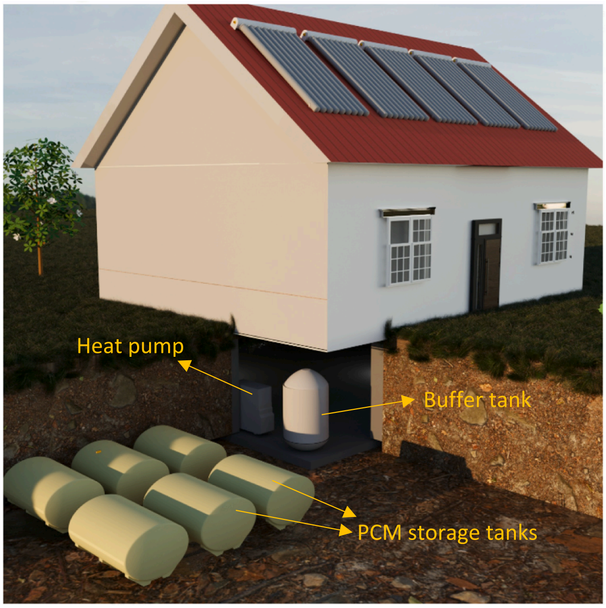

a) Concept of SAHP-SAT

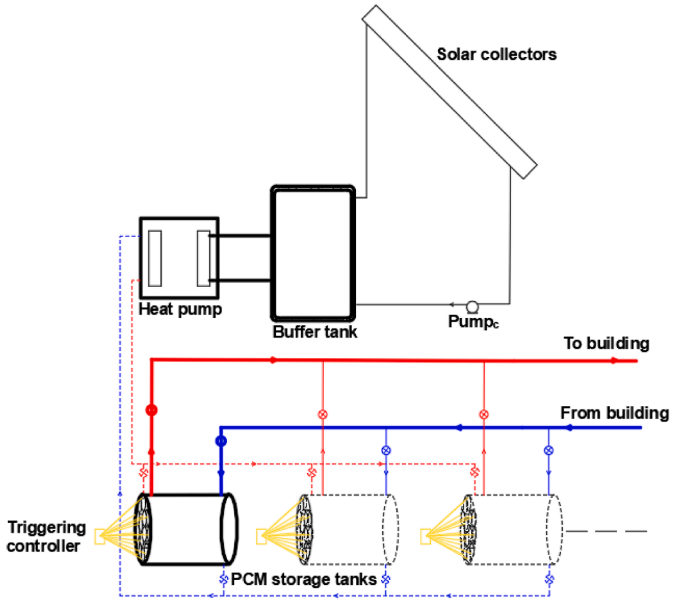

b) Schematic view

Fig. 1. (a) Concept view of the SAHP-SAT system; **(b)** Schematic view of solar assisted heat pump system with crystallisation-controllable PCM storage units (SAHP-SAT).

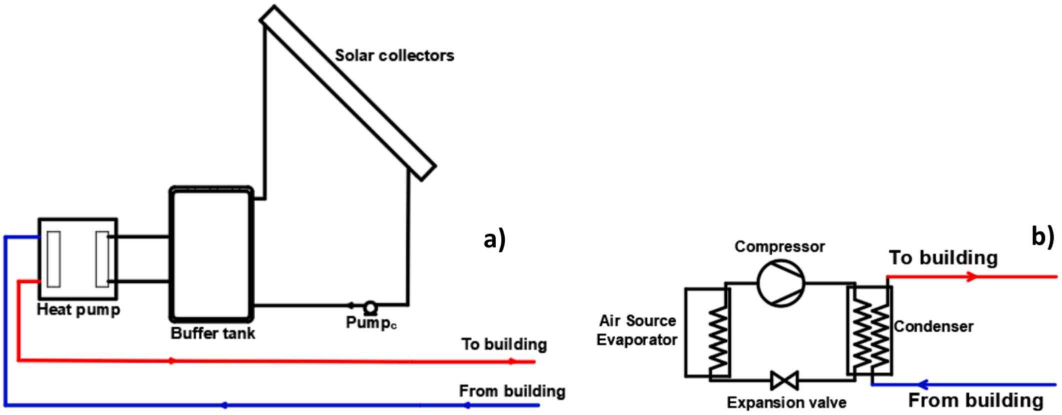

Fig. 2. Schematic of other counterpart systems for comparison with SAHP-SAT: **a)** Conventional solar assisted heat pump (SAHP); **b)** Conventional air source heat pump (ASHP).

buffer tank, and the heat pump provides the required heat to the building using the heat from the buffer tank as a source. The solar collector pump operates during solar hours, whereas the heat pump runs according to the building's heating demand. The system benefits from higher performance, but its operation time and electricity consumption are aligned with the heating profile which would bring additional stress on the grid during peak times.

Heating demand: The performance of the proposed unit is dependent on the heating profile of the building. Therefore, the hourly heating demand profile of a case study building is considered. This case involves a building located at the University of Nottingham's Park Campus, one of the Creative Energy Homes. Designed as a low-carbon building, it is more energy-efficient compared to standard Victorian houses in the UK. The building's thermal model was established using IESVE software [35], and details of the thermal model and building fabrics can be found in a previous study [11]. The same model has been used in this paper to ensure consistency and facilitate clear comparisons. However, this time, the domestic hot water consumption profile was included, accounting for a demand of 30 Liters per person. The building is a two-story structure with dimensions of 7.9 m × 7.9 m × 5.0 m, featuring an interior floor area of 62.41 m^2 for each floor. The occupancy, heating, ventilation, appliances, and lighting profiles are designed for four residents. Using weather conditions from Nottingham, UK, selected one-week profiles of solar irradiance, ambient temperature, and heating demand are presented in Fig. 3.

The chosen week presents a suitable daily solar variation profile for this study, as the solar irradiance is low on the second and the last day, reaching a maximum of 150 W/m^2. Consequently, the system can utilize the reserved SAT tank instead of the solar heat pump on days with low solar irradiance. Later, when the solar irradiance is relatively higher, the reserved SAT tank is recharged and prepared for future low-solar days. The heating demand profile given in Fig. 3b is influenced by the ambient temperature, which varies and drops to -2 °C. Thus, daily heating demand varies from 20.4 kWh to 48 kWh, a total of 245 kWh for one week.

2.1. Controlled crystallization mechanism and triggering controller

Supercooling is a phenomenon in which a PCM remains in a liquid state even when its temperature drops below its solidification point. Although supercooling is often considered undesirable because the stored latent heat is not released at the designated temperature, it can be beneficial when controlled correctly. In an uncontrolled state, supercooled PCMs can release stored latent heat randomly upon spontaneous solidification, making thermal management unpredictable.

However, when crystallization can be externally controlled, supercooling becomes a valuable feature for short- to mid-term heat storage applications. Controlled crystallization allows the stored latent heat to remain preserved until it is needed, releasing heat on demand rather than unpredictably. This preservation of latent heat means that the PCM only loses its sensible heat during the supercooled phase, significantly reducing heat losses from the storage unit over time.

As demonstrated in Fig. 4, two well-insulated, overall heat loss coefficient of the tanks is given as 1.13 W/m^2K [36], identical PCM storage tanks under a 10 °C ambient temperature over eight days are compared to illustrate the benefits of controlled crystallization. One tank uses a PCM without supercooling properties, while the other uses the PCM with controlled supercooling. In simulation, both units start at 70 °C after reaching a fully melted state. By the second day, the conventional PCM begins to solidify and gradually loses its available latent heat, fully depleting by the eighth day. In contrast, the supercooled PCM remains

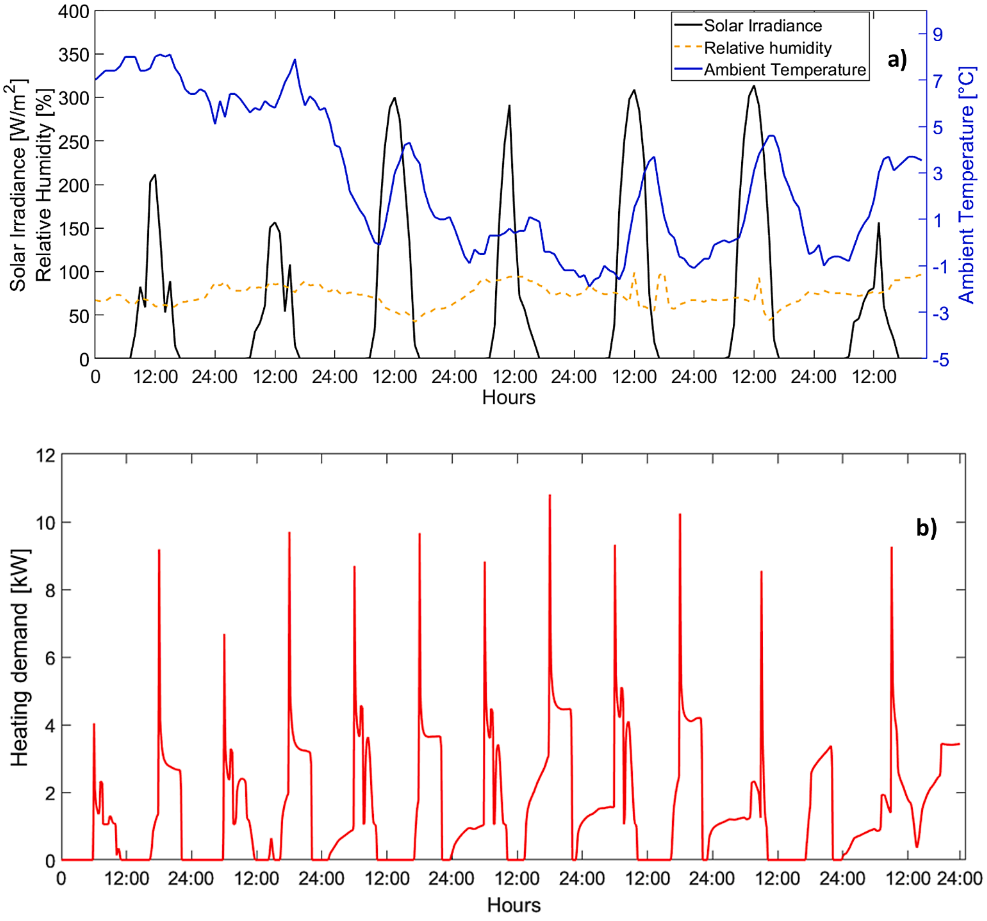

Fig. 3. Weather data and heating profiles (05 February to 11 February), **a)** Solar irradiance and ambient temperature profile, **b)** Heating demand profile.

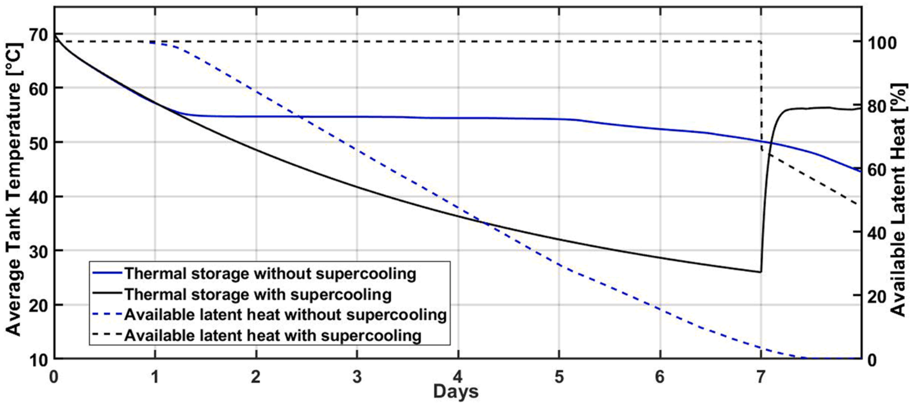

Fig. 4. Comparison of controlled supercooling and conventional without supercooling storage tanks storage ability.

liquid, losing only sensible heat as its temperature drops. It is then triggered after seven days, raising the tank temperature to 55 °C, with about 60% of its available latent heat preserved due to reduced heat loss. This highlights the advantage of controlled crystallization in preserving stored energy until it is needed. By using controlled supercooling, the system can reduce heat loss, maintain a higher energy storage capacity, and offer on-demand heat release, making it an efficient strategy for thermal energy storage applications.

In order to inducing nucleation in supercooled SAT, several methods for have been explored, including crystal seeding, local cooling, percussive vibration, and electric triggering. Among these, adding SAT crystals is commonly used due to its reliability, though it often requires manual intervention. Other methods, such as local cooling with liquid CO_2 or Peltier devices, as well as percussive vibration, have also shown effectiveness in inducing nucleation [5]. For practical applications in buildings, automatic triggering that aligns with heating demands is essential. Electric triggering offers a cost-effective, easily automated method for controlling the release of stored energy in supercooled SAT. This method involves generating an electric field through electrodes, which induces a concentration gradient in the SAT and initiates nucleation. In previous work [22], a graphite cathode (−) and a silver anode (+) were chosen for electric triggering. After preparing the triggering unit, it was immersed in a PCM tube, and a 9 V voltage was applied. The nucleation process began, and the PCM temperature rapidly increased from 29.5 °C to 58 °C.

As it is seen from the simulation result, although reserving the SAT tank for subsequent days shows promise for solar energy management with less heat loss, the available latent energy of the PCM after triggering is influenced by the degree of subcooling and must be included in simulations. Assuming the triggering temperature of the tank is 20 °C, up to 40% of the latent heat could be lost despite the temperature reaching 58 °C. This scenario is only possible if the SAT storage remains in the container as a reserve tank for more than ten days in given conditions. In the reference paper [22], the best-fit equation for available latent heat, considering the initial PCM temperature before crystallization triggering, is given in Eq. (1):

$$h_{fusion} = 98.7 + 2.9 \bullet T_{initial} \tag{1}$$

Based on the information provided and the system description, a simulation is conducted following the outlined operation strategy. The operation method for the three SAT tanks is shown in Fig. 5, taking into account daily solar irradiance profiles. The choice of three tanks was made to present the proposed method. While two tanks provide basic flexibility, adding a third tank offers significant advantages, such as allowing one tank to act as a reserve during extremely low solar energy periods. This configuration helps maintain continuous heating without interruption or the need for auxiliary heating elements. Although more tanks could enhance performance over multiple consecutive low solar energy days.

Regardless of the solar profile, one SAT tank is triggered at midnight to provide heating to the building until its supply temperature drops to 40 °C. This SAT tank is designed to offer a minimum of 13 kWh of heat storage, ready for use at 58 °C (assuming a 20 °C reserve tank temperature). When solar irradiance is sufficient, the solar assisted heat pump unit charges the SAT tank during solar hours, while the triggered tank continues to provide heat to the building. The HP charging temperature is set to a maximum of 70 °C, which is the heat pump’s maximum supply temperature. Thus, after charging, the SAT tank’s water temperature will be 70 °C in the evening. To utilize this high temperature, the tanks are shifted in the evening when the building requires the most heating. It is anticipated that this arrangement will provide sensible heating to the building until midnight, at which point the SAT PCMs are activated, reaching a temperature of 58 °C.

In an ideal scenario, these two tanks switch according to the given operation strategy. However, on days with low solar irradiance, recharging the SAT tank may be inefficient. On such days, the system

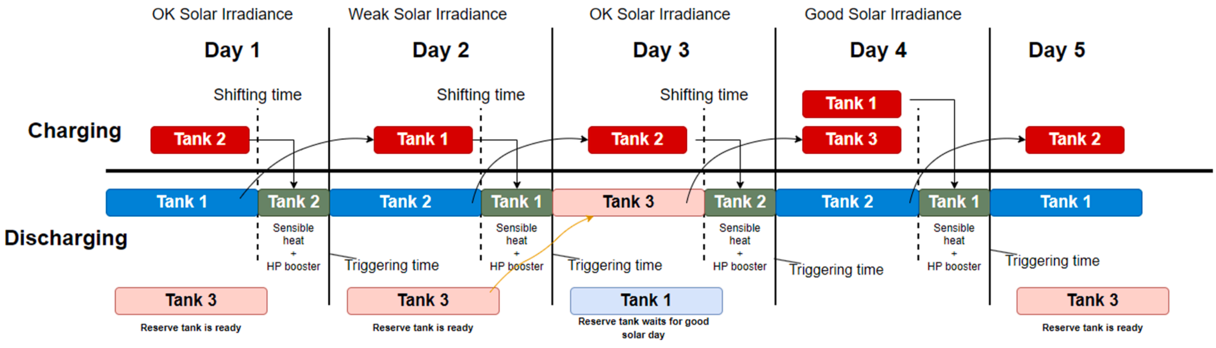

Fig. 5. Operation method with three PCM storage tanks.

does not charge the SAT tank, and solar collectors slightly increase the buffer tank's temperature. This increase positively affects the system's performance on the following day. Nevertheless, the heat pump continues to provide sensible heating to the SAT tank for the evening shift. Since the PCM charging does not occur, the reserved SAT tank is connected to the supply line and triggered at midnight. Depending on solar availability, the usual tank is then charged. On subsequent days, when the solar irradiance profile is high, the usual operation resumes, and both the tank and the discharged reserve tank are charged together efficiently. The details of the operation and simulation results will be presented and discussed in the results section.

The charging operation proceeds as follows: To facilitate electricity demand shifting, the SAHP begins operation at 9 AM. However, the controller must make a decision, as it has the option to operate in one of three modes: usual one-tank charging, two-tank charging, or low operation mode.

The one-tank charging mode is the standard operation for the SAHP, providing a maximum of 7 kW of heating to the SAT tank. However, this heating output decreases over time as the SAT temperature increases, leading to limited heat transfer as the temperatures of the system components converge. During this operation, if the solar irradiance is weak, the buffer tank temperature drops, and if the solar irradiance is strong, the buffer tank temperature rises.

In the low operation mode, both solar irradiance and buffer tank temperature must be below certain threshold values, and the SAHP supplies only 1 kW of heat to the tank. This heat is insufficient to charge the PCMs but serves to slightly increase the tank's sensible heat capacity. In this mode, the buffer tank temperature is expected to remain the same or increase slightly.

The two-tank charging mode is activated only when both the solar irradiance and buffer tank temperature exceed predetermined values.

Fig. 6 shows the flowchart of the charging mode decision. The system's operation is based on the estimated maximum solar irradiance and the buffer tank's temperature. An upper threshold for solar irradiance of 280 W/m^2 has been set. If the irradiance exceeds this value and the buffer tank temperature is also above 30 °C, the system is capable of charging two tanks. Conversely, if the estimated solar irradiance falls below 200 W/m^2 and the buffer tank temperature is below 20 °C, the system switches to low mode. In scenarios not covered by these conditions, the SAHP operates by charging a single tank as standard.

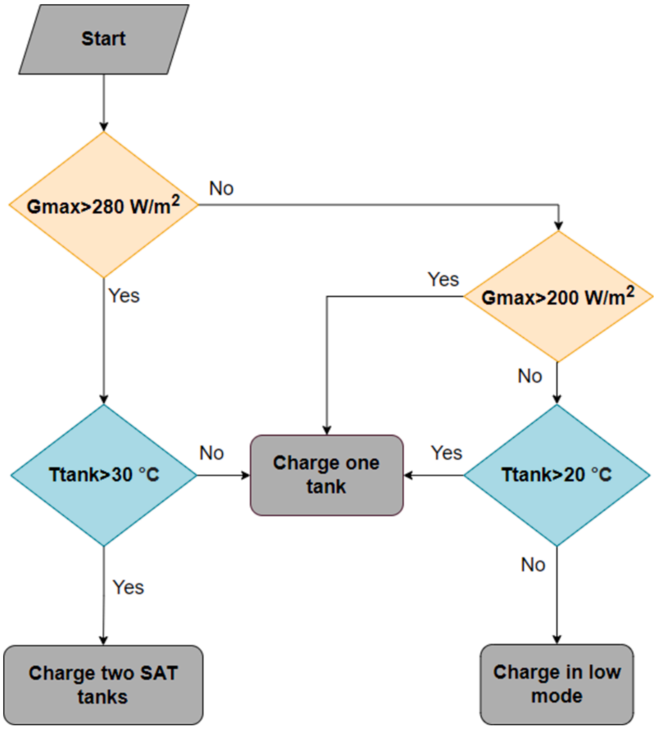

Fig. 6. Charging mode decision flow chart.

3. Modelling of system components

In this section, mathematical models of solar thermal collectors, buffer tank, heat pump and PCM heat storage units are given.

3.1. Solar thermal collectors

The thermal collector modelling is conducted assuming under quasi-steady state conditions and steady-state equations are used neglecting the thermal capacity of the collector. Evacuated tube heat pipe collector was chosen for their good thermal performance even in cold ambient conditions [37].

$$\eta_{th} = 0.556 - 0.888 \bullet \frac{T_m - T_a}{G} - 0.006 \bullet \frac{(T_m - T_a)^2}{G} \tag{2}$$

Where T_a is ambient temperature, T_m is mean temperature of the fluid inside the collector and G is solar irradiance. The collected heat by the solar collector increases the heat transfer fluid (HTF) temperature at the exit of the collector. Eq. (3) is given to calculate the collected useful heat.

$$\dot{Q}_{\text{solar}} = \eta_{th} \bullet A_{col} \bullet G \tag{3}$$

Where A_{col} is total collector area. The collected heat is transferred to the heat transfer fluid by using Eq.(4):

$$\dot{Q}_{\text{solar}} = \dot{m}_{HTF} \bullet c_{p,HTF} \bullet (T_{col,e} - T_{col,i}) \tag{4}$$

$T_{col,e}$ and $T_{col,i}$ indicate the temperature of the HTF at the exit and inlet of the collector, respectively. $\dot{m}_{HTF}$ and $c_{p,HTF}$ represent the mass flow rate and specific heat capacity of the HTF. In this study, an ethylene glycol–water mixture is used as the HTF on the collector side to prevent freezing under cold ambient conditions. The HTF flows from the buffer tank into the collectors and then returns to the buffer tank at a higher temperature.

3.2. Buffer tank

The buffer tank maintains the stored solar heat for the heat pump which is used as the heat source. Its temperature significantly influences the performance of the heat pump; thus, the charging and discharging of the tank need to be modelled. The buffer tank undergoes charging by solar collectors and discharging by the heat pump during their operation. Additionally, ambient heat losses impact the temperature of the tank. The transient performance of the buffer tank is modelled using the energy balance equation for an unstratified tank [38], aiming to reduce computational time.

$$m_t \bullet c_{p,HTF} \bullet \frac{dT_t}{dt} = \dot{Q}_{\text{solar}} - (UA)_t \bullet (T_t - T_{room}) - \dot{Q}_{eva} \tag{5}$$

Where, T_t is tank temperature and $\dot{Q}_{eva}$ indicates the heat taken by the heat pump's evaporator. The remaining parameters represent heat loss to the environment. U is overall heat loss coefficient and it is assumed as 0.8 W/m^2, assuming well insulated cylinder [39].

3.3. Heat pump

The heat pump consists of four main components: the compressor, condenser, expansion valve, and evaporator. In the modelling, the condensation temperature is limited to 70 °C, as this is the upper level for common commercial heat pumps. Consequently, the hot water supply temperature to the building by ASHP and SAHP can reach approximately 60 °C. This temperature is also sufficient for charging the

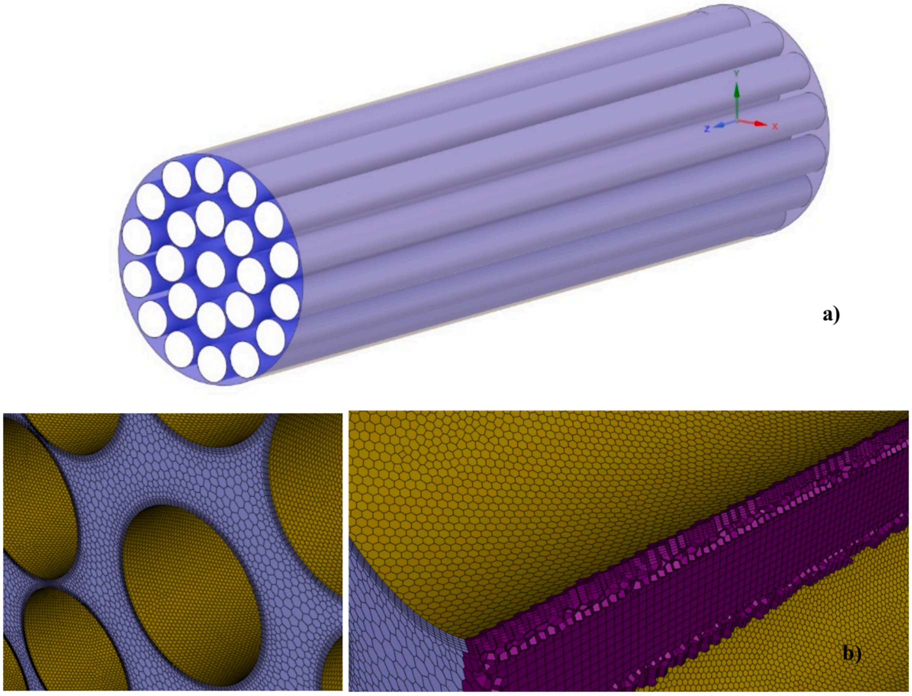

Fig. 7. PCM storage tank CFD solution domain **(a)**, and applied meshes **(b)**.

SAT tanks. Conversely, the evaporation temperature is dependent on the buffer tank temperature, which significantly influences the compressor's power consumption. The COP of the heat pump is defined as follows:

$$\mathrm{COP} = \frac{\dot{Q}_{cond}}{\dot{W}_{comp}} \tag{6}$$

Where $\dot{W}_{comp}$ and $\dot{Q}_{cond}$ are compressor consumption and condenser load, respectively. The following assumptions are made for the heat pump simulation: For the ASHP system, the evaporation temperature is assumed to be 10 K lower than the ambient temperature [40]. For the SAHP system, a 5 K pinch temperature difference approach is assumed to ensure proper heat transfer from the buffer tank to the refrigerant in the evaporator [19]. In all systems, the degrees of superheating in the evaporator and subcooling in the condenser are assumed to be 3 K. The details of heat pump modelling are given in Appendix A1.

An important consideration for ASHP systems is defrosting when the ambient temperature falls below 2.5 °C and the relative humidity exceeds 70%. An empirical equation from Roccatello et al.[41] is used to account for defrosting phenomena during the operation of ASHP. They conducted experiments at ambient temperatures ranging from 2.5 °C to −4 °C and relative humidities of 70%-80% and 90%. The equation is as follows:

$$COPdrop = a + b \bullet RH + c \bullet T_{am} + d \bullet RH \bullet T_{am} + e \bullet T_{am}{}^{2} + f \bullet RH \bullet T_{am}{}^{2} + g \bullet T_{am}{}^{3} \tag{7}$$

Where the coefficients in the correlation are $a = 15.05$, $b = -0.2543$, $c = 0.01351$, $d = -0.007022$, $e = 0.4319$, $f = -0.005945$, $g = 0.03681$.

3.4. Heat storage tank

The PCM storage tanks in this study were designed using cylindrical containers rather than spherical capsules, despite the well-known advantages of spherical shapes in enhancing heat transfer due to their higher surface area-to-volume ratio. The PCM storage unit consists of a cylindrical container holding several cylindrical PCM tubes. Controlled crystallisation requires triggering devices to initiate crystallization and effectively release stored heat. Thus, cylindrical containers were chosen to provide an efficient balance between heat transfer and system control. The storage unit is designed with a horizontal configuration to optimize thermal performance and reduce potential material degradation issues. The chosen PCM, SAT, is a salt-based phase change material known for its tendency to experience phase separation particularly in vertical configurations. As it was reported that [42] the vertical setup can experience up to an 8.2% decrease in thermal capacity due to phase segregation. Therefore, the unit is oriented horizontally and segmented into 'n' distinct control volumes. For the purpose of analysing temperature gradients and heat transfer processes, the assumption is made that mass transport within the tank is one-dimensional. Consequently, the length of the tank is divided into nodes, with the energy balance equations for all nodes being solved simultaneously. Furthermore, the PCM tubes themselves are segmented into radial nodes to enable the analysis of heat transfer from the PCM's centre to its outer edges. The SAT unit was modelled and validated in the reference paper [11]. The same assumptions for SAT unit modelling were applied in this study. The discretized heat transfer model for PCM storage tank is given in Fig. A1 in Appendix A2.

The entire system simulation, including all components such as the solar collectors, pumps, buffer tank, heat pump, and PCM tank, was conducted using MATLAB. Each component model was developed in MATLAB to allow for integrated system-level analysis, optimization, and control strategy evaluation. However, as the tank arrangement is not a standard arrangement, convective heat transfer coefficients between the heat transfer fluid and the PCM tubes within the storage tank is needed to be accurate. Thus, Computational Fluid Dynamics (CFD) analysis was performed to model and find the heat transfer coefficient between the water and the PCM tubes, later, this heat transfer coefficient was incorporated into the overall model for comprehensive analysis.

23 PCM tubes are inserted in the tank based on a combination of factors: Achieving the required PCM mass, minimizing the number of triggering devices, optimizing heat transfer, and ensuring efficient melting times. The system was designed to charge during the day to maximize the use of solar energy, and thus the diameter of the PCM tubes was chosen as 8 cm to ensure complete melting within the

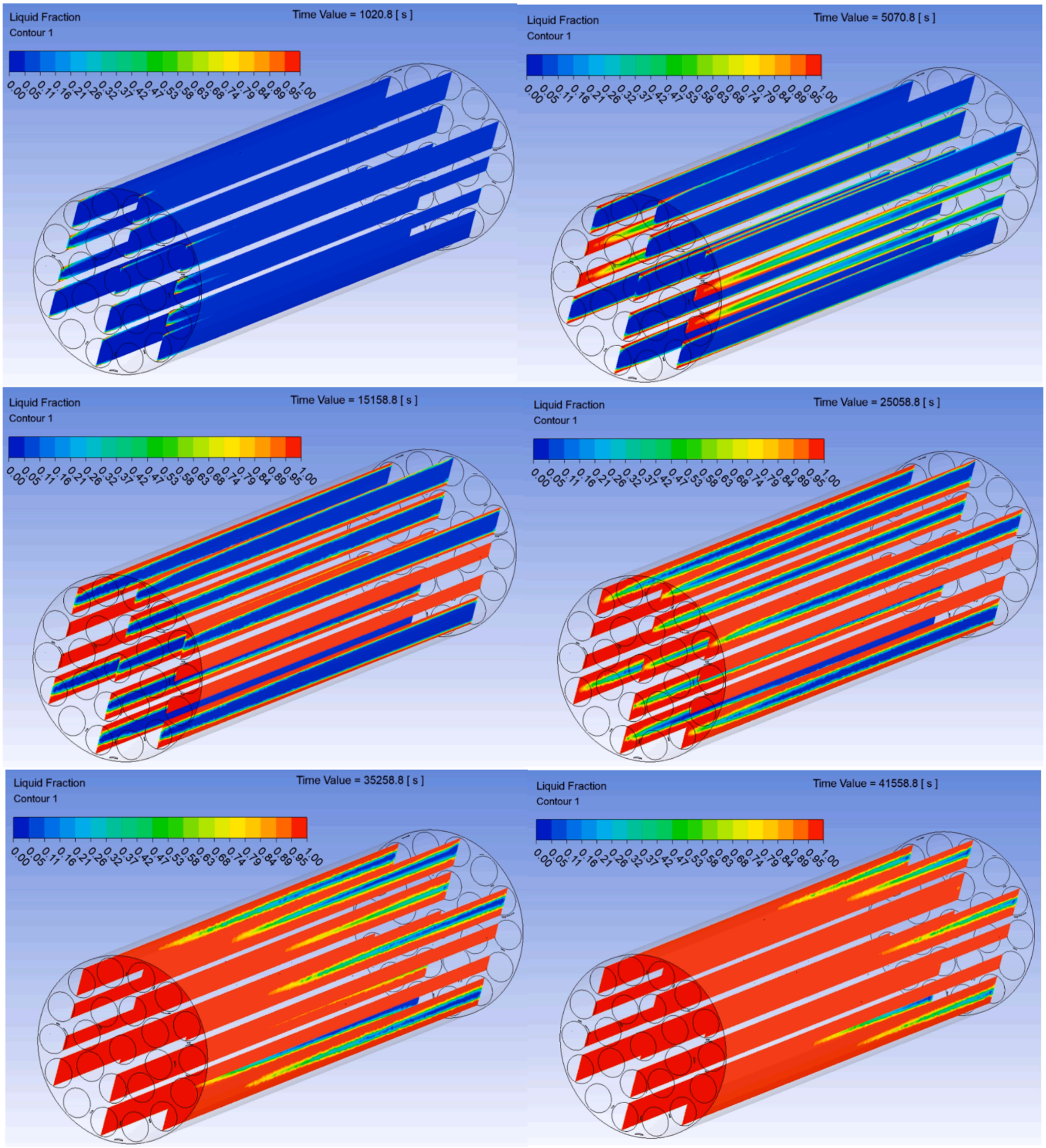

Fig. 8. The liquid fraction distribution in the tank at different times during charging.

available charging time. For the targeted energy storage of approximately 20 kWh per PCM tank, the number of cylinders was determined to provide the necessary thermal capacity while maintaining manageable heat transfer dynamics. The PCM storage tank is given in Fig. 7a. Initially, the Ansys design modeler was employed to depict the geometry of the computational domain, followed by the application of mesh to the geometry using ANSYS Meshing. Numerous attempts were made for discretization, and the most suitable one, as illustrated in Fig. 7b, is chosen. Poly-hexcore cell structure and inflation were applied near the wall to refine grids

The analysis is based on several assumptions: the flows considered are incompressible, unsteady, and laminar. Additionally, it is assumed that the thermophysical properties of the fluid remain constant throughout, and effects such as buoyancy and radiation are neglected.

To demonstrate the reliability of the numerical study and validate the numerical solution for the heat transfer coefficient, the study by Taborek [43] was used for the staggered arrangement. The geometry was modified to align with the reference, and the CFD settings were validated using the provided equations. After validation, the tank geometry, as shown in Fig. 7, was applied, and the PCM solution methods were implemented.

In PCM solutions, generally, equivalent heat capacity method, enthalpy method and temperature transforming model are suggested [44]. The enthalpy-porosity method is used for modelling the melting process of PCM units. The governing equations are given below [45]:

The continuity equation:

$$\nabla^2\vec{V} = 0 \tag{8}$$

The conservation of momentum equation:

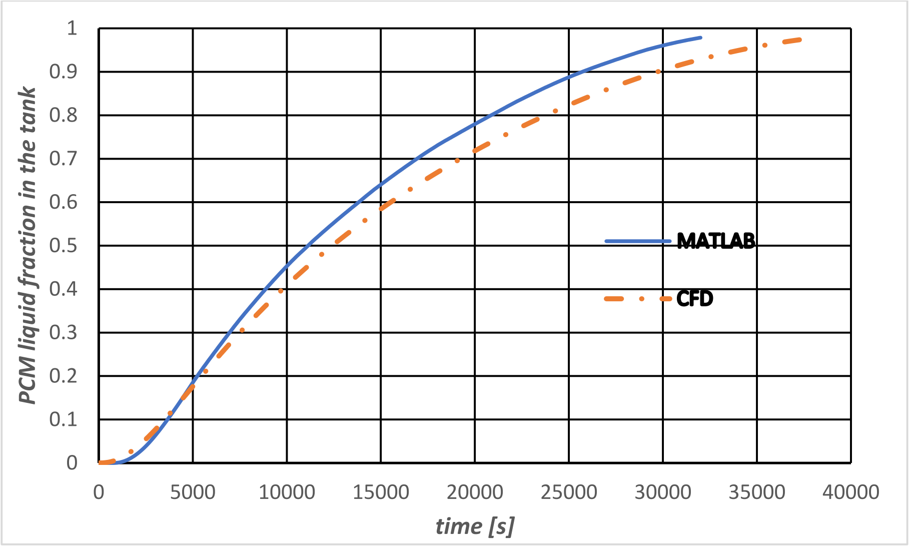

Fig. 9. The comparison of MATLAB model and CFD results of liquid fraction change during charging process.

$$\rho\frac{\partial\vec{V}}{\partial t}+\rho\left(\vec{V}\nabla\right)\vec{V}=-\nabla P+\mu\nabla^{2}\vec{V}+\rho\beta\vec{g}(T-T_{0})+\vec{S} \tag{9}$$

The conservation of energy:

$$\frac{\partial}{\partial t}(\rho He)+\nabla\bullet\left(\rho\vec{V}H\right)=\nabla\bullet(k\nabla\mathrm{T}) \tag{10}$$

Where the specific enthalpy (H) of the PCM is the sum of its sensible enthalpy (h_{sen}) and latent enthalpy (h_{lat}). Eq. (11) is given for enthalpy.

$$H=h_{sen}+h_{lat} \tag{11}$$

Where, sensible heat is:

$$h_{sen}=he_{o}+\int_{T_{o}}^{T}C_{p}dT \tag{12}$$

The latent enthalpy during the phase change is given in Eq. (13).

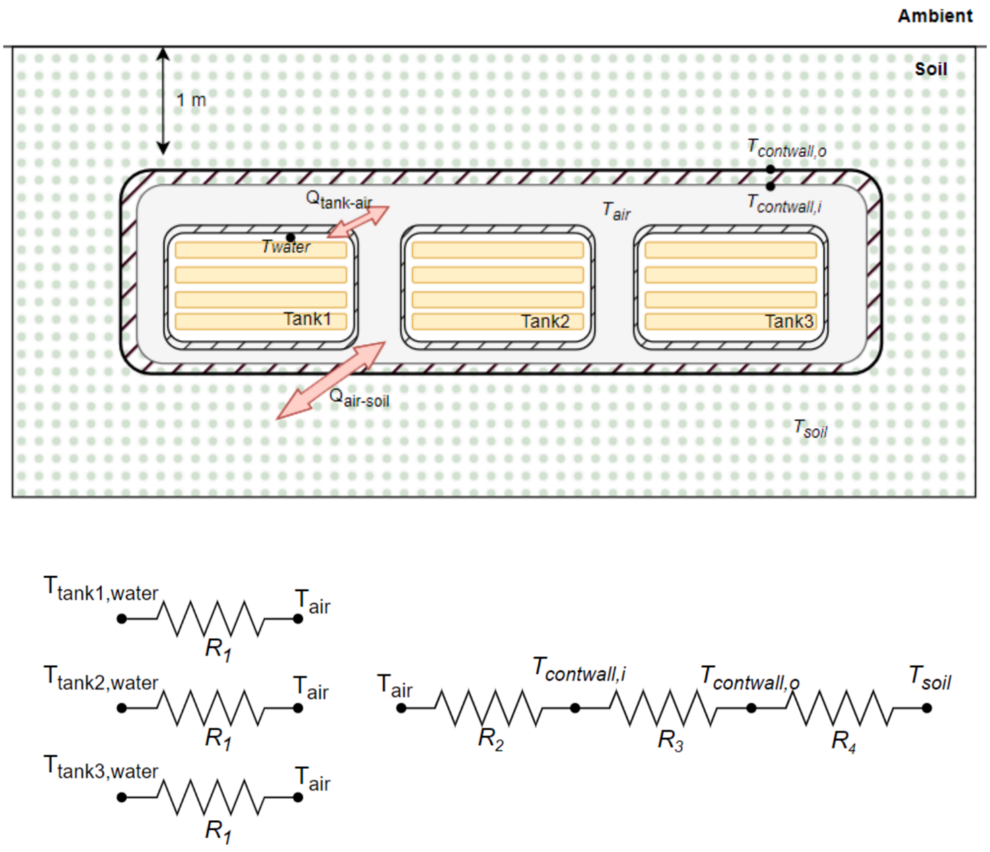

Fig. 10. Underground container heat transfer diagram.

$$h_{lat} = \lambda \bullet \Delta L \tag{13}$$

where ΔL is the latent heat of fusion of the PCM, and λ is the liquid fraction,

$$= T < T_{solid}$$

$$\lambda = \frac{T - T_{solid}}{T_{liquid} - T_{solid}} T_{solid} < T < T_{liquid}$$

$$= T > T_{liquid} \tag{14}$$

Second-order upwind scheme and PRESTO scheme are used to solve momentum equations and pressure equations. The SIMPLE algorithm was used for the pressure velocity coupling. The under-relaxation factors for the velocity components, liquid fraction, pressure, and energy are set at 0.7, 0.9, 0.3 and 1, respectively [45]. The convergence criteria for continuity and momentum equations residuals are set below 10^{-5}, with the energy equation's residual being below 10^{-9}, respectively.

The boundary conditions are explained as follows: A constant mass flow rate (0.2 kg/s) and constant temperature are provided at the computational domain's inlet section for a given Reynolds number. The wall adheres to the no-slip wall condition. A pressure outlet boundary condition is set at the outlet section, with the outlet pressure adjusted to gauge pressure "0". After conducting the study, the Reynolds number is written as:

$$\mathrm{Re} = \frac{\rho u D_h}{\mu} \tag{15}$$

where the hydraulic diameter is defined as:

$$D_h = \frac{4 \bullet Wettedarea}{WettedPerimeter} \tag{16}$$

The average heat transfer coefficient is obtained by:

$$\mathrm{h} = \frac{\dot{q}}{\Delta T_{lm}} \tag{17}$$

Here the heat flux $\dot{q}$ and logarithmic mean temperature difference ΔT_{lm} are taken from the numerical solution.

Fig. 8 provides a detailed breakdown of fraction distributions, offering additional insights into the simulation outcomes. The figure represents the charging process, which refers to hot water coming from the heat pump unit. The initial temperatures of both the water and PCM are set to 40 °C. The inlet mass flow rate and water temperature are set to 0.2 kg/s and 70 °C, respectively. A pressure outlet is applied at the outlet section, and an overall heat transfer coefficient of 1.13 W/m^{2}K is applied at the outside of the tank. The initial time step size is set to 0.01 s to ensure convergence. The visual representation in Fig. 8 enhances the understanding of the system dynamics, particularly in relation to the distribution of fractions during the analysed processes. This analysis further strengthens the reliability of the model and its ability to capture intricate details in the studied phenomenon. As seen here, the melting process is not uniform. This non-uniformity could potentially be a key aspect to consider in further refining the model or understanding the underlying physical phenomena.

Fig. 9 illustrates the increase in the PCM liquid fraction during a standard charging period in the tank, as simulated by two different software tools. This demonstrates that the MATLAB model can reasonably simulate the charging behaviour of the PCM tank, provided that an accurate convective heat transfer coefficient is applied. Although the MATLAB model uses larger node sizes compared to the detailed CFD analysis, the results show good agreement with the CFD findings.

As the PCM tanks are buried underground in a container, heat loss analysis is necessary considering energy balance equations to obtain temperature of the reserve tank. Fig. 10 is given to show heat transfer diagram of the underground container. In this simplified configuration, it is assumed that the examined three tanks have contact with container air, meaning heat is transferred between each tank to container air or air to tank. Assuming the container is in 1 m buried in the soil, another heat transfer is happening between the container air to soil.

Container air temperature is assumed as uniformly distributed in the container to simplify the analysis. The container dimensions are determined as 2 m x 2 m x 1 m. R_2, R_3 *and* R_4 are given as 0.125 (natural convection), 0.151 (plastic container) and 0.1124, respectively. Thermal resistance from soil to container outside surface (R_4) is found from EES software's conduction shape factors under heat transfer and fluid flow function using soil conductivity [46]. The soil temperature is taken as 10.6 °C from British geological survey by natural environment research council's estimated mean soil temperature in the UK [47].

Table 1
System specifications of ASHP and SAHP.

ASHP		SAHP	
Parameter	Value	Parameter	Value
HP condensation temperature	70 °C	Solar collector area	50–40 m^2
Evaporation temperature	T_{am} −10°C	Collector flow rate	0.033 kg/s per collector
Condenser output (SAHP and ASHP)	Heating demand of the building	Buffer tank to HP flow rate	0.33 kg/s
		Pinch temperature in HP evaporator	5 °C

4. Results and Discussions

This numerical study aims to present a comparison of different systems' performance considering their energy consumption and grid load hours. Therefore, Nottingham weather data for seven days in February and the building's heating demand profile based on IESVE simulation results were used referring to Fig. 3.

4.1. Conventional air source and solar-assisted heat pumps

Before the evaluation of the PCM storage tank, conventional solar assisted heat pump unit performance is investigated in this section in order to present the effect of solar energy utilization. The advantage of solar assisted heat pump unit is having a better COP since it stores solar energy in a buffer tank which has a higher temperature than the ambient air temperature. However, one of the drawbacks of the solar assisted heat pump unit is requires a large buffer tank size in order to operate even on nights. Thus, in this section, ASHP and SAHP performances are compared for a period of one week. Limitations and advantages of buffer tank size will be discussed. Specifications for both systems are given in Table 1.

In order to investigate the effect of buffer tank size, a parametric study was conducted. Fig. 11a displays the results from using different buffer tank volumes and 40 m^2 and 50 m^2 collector areas, illustrating the temperature variations within the tank over a week and allowing for comparisons with the ambient temperature. As the buffer tanks undergo charging and discharging loads throughout the day, larger tanks experience less temperature fluctuation than smaller ones. This is because the heat capacity of a larger tank is greater, resulting in a more moderate temperature increase from solar energy utilization and a limited temperature decrease during the use of a heat pump. Moreover, it is obvious that the collector area influences the amount of solar energy harvesting, thus, a 50 m^2 collector area results in a higher temperature increment compared to a 40 m^2 collector area for the same volume of buffer tank. As evident from Fig. 11a, the temperature of the largest buffer tank ranges from a minimum of 10.74 °C to a maximum of 34 °C for a 50 m^2 collector area, 6 °C and 25.6 °C for a 40 m^2 collector area. Whereas the smallest tank's temperature spikes to 52.7 °C and 40 °C and drops to −2 °C and −8 °C, for 50 m^2 and 40 m^2 collector areas, respectively. Clearly,

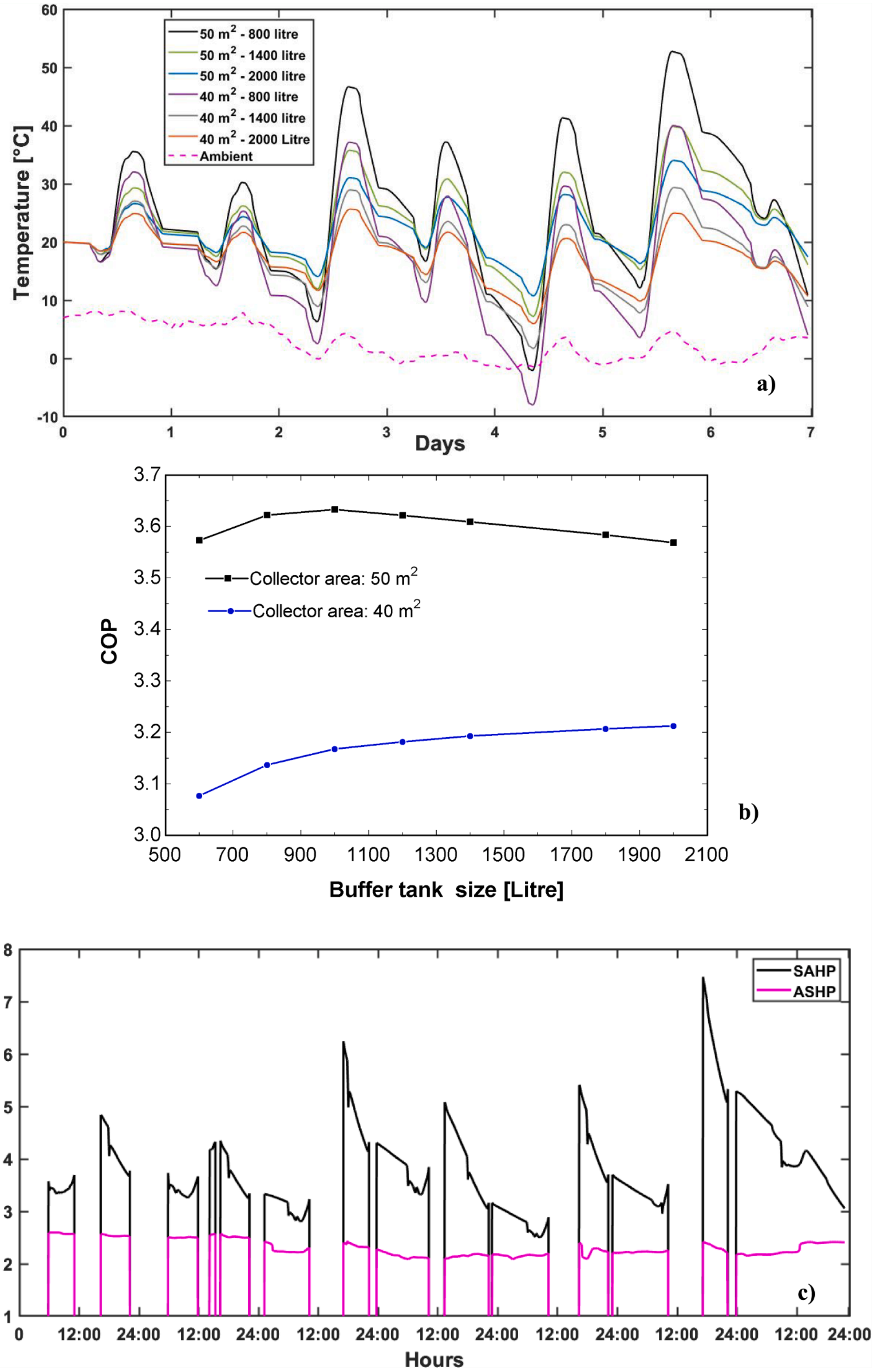

Fig. 11. **(a)** temperature variations of buffer tank of different volumes; **(b)** the effect of buffer tank sizes on weekly COP of SAHP; and **(c)** COP variations of ASHP and SAHP (50 m^2-1000 L).

these temperature variations would affect the system's COP. Therefore, Fig. 11b is provided, showing the effects of different buffer tank volumes and collector areas on the COP over a week-long operation.

Using a larger buffer tank results in an increased weekly COP, even though the maximum temperature is lower than that of a smaller tank. This improvement aids solar utilization, owing to the higher thermal efficiency of the solar collector facilitated by the lower temperature of the buffer tank. Moreover, the larger heat capacity of the buffer tank prevents performance drops during periods of higher heating loads. As depicted in Fig. 11b, increasing the buffer tank volume from 600 L to 2000 L results in a performance improvement of only 4.4% when using a 40 m^2 collector area. The trend also indicates that while the COP of the system can be further increased with larger buffer tanks, the rate of improvement diminishes.

For a 50 m^2 collector area, the highest COP is observed with a 1000 L buffer tank volume. Although smaller volumes allow the buffer tank temperature to reach higher levels, during weeks with low solar days, their temperature significantly drops, reducing the weekly COP. Conversely, with larger volumes, although the temperature does not drop on low solar days, the increase in temperature is also limited, resulting in a slightly lower weekly COP. Therefore, a 1000 L buffer tank has been selected for the SAHP application in this study to balance the

Table 2
Design specifications of SAHP-SAT system.

Parameter	Value	Parameter	Value
Stored heat in one tank	13 kWh – 22 kWh	Solar collector area	50 m^2
Total SAT mass in tank	301.6 kg	Collector flow rate	0.033 kg/s per collector
Total PCM volume in tank	208 Liters	Heat Pump output	Maximum 7 kW
Water mass in tank	150 kg	H.P. condensation temperature	Maximum 70 °C
Buffer tank	1000 Liters	Pinch temperature in H.P. evaporator	5 °C
Buffer tank fluid	Ethylene Glycol water mixture (30 %)	Flow rate between buffer tank and HP	0.33 kg/s
Number of PCM tubes in tank	23	Tank heat loss coefficient	1.13 W/(m^2 • K) [36]
PCM volume in one tube	9 Liters	SAT Specific heat	2.9/3.1 kJ/(kg • K) [5]
SAT latent heat	264 kJ/kg [5]	SAT density	1450 kg/m^3 [5]
SAT thermal conductivity	0.6/0.385 W/(m • K) [5]	SAT kinematic viscosity	5.81 mm^2/s [5]

space requirements and achieve optimum performance for a 50 m^2 solar collector area.

Fig. 11c illustrates the COP variations between the ASHP and the predetermined SAHP system. The COP of the ASHP appears more stable compared to that of the SAHP when the ambient temperature variation is less than 10 °C. Over a seven-day period, taking into account the compressor consumption and the heating provided by the condenser, the COP for the ASHP is calculated to be 2.34, including defrosting. In contrast, the SAHP's COP is 3.63, utilizing a 50 m^2 collector area and a 1000 L buffer tank. Although the figure shows that the instant COP of the SAHP can exceed 7, this does not reflect the overall performance as it could be attributed to significantly low heating capacity. Therefore, the weekly COP should be considered, taking into account the weekly heating and compressor consumption.

4.2. Solar-assisted heat pump with crystallisation-controllable system operation

The operation of the solar-assisted heat pump with a controllable SAT system was discussed in Section 2. Since each charged SAT tank is expected to provide heating to the building for at least 18 h, its sizing is crucial to avoid the need for auxiliary heating or oversizing of the unit. However, the heating demand from the building varies according to many factors, especially the ambient temperature variation. As the dischargeable heat storage capacity depends on the activation temperature, a designed SAT tank can provide a minimum of 13 kWh of heating when the initial temperature is 20 °C, and up to 22 kWh when the activation temperature is 57 °C. To achieve these specified capacities, the SAT tank volume has been determined to be approximately 350 L, consisting of around 200 L of SAT PCM and 150 L of water. The details of the components and system specifications are provided in Table 2.

The heat discharging operation proceeds as follows: The charged SAT tank is connected to the building's heating system in the evening to provide heating through its sensible heat. When the tank's temperature drops to 40 °C or when midnight arrives, the PCM tubes are activated and begin to release their latent heat. This process of heating continues

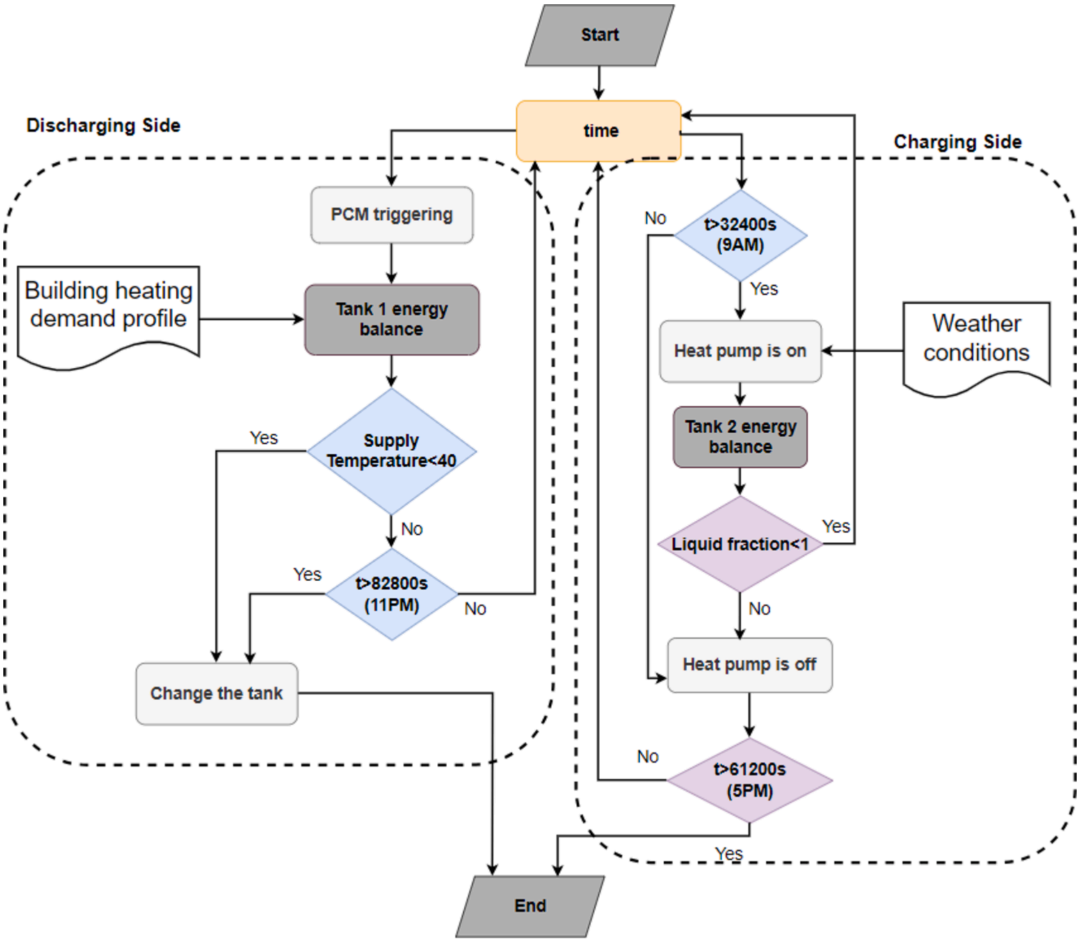

Fig. 12. Flow chart of one day system operation.

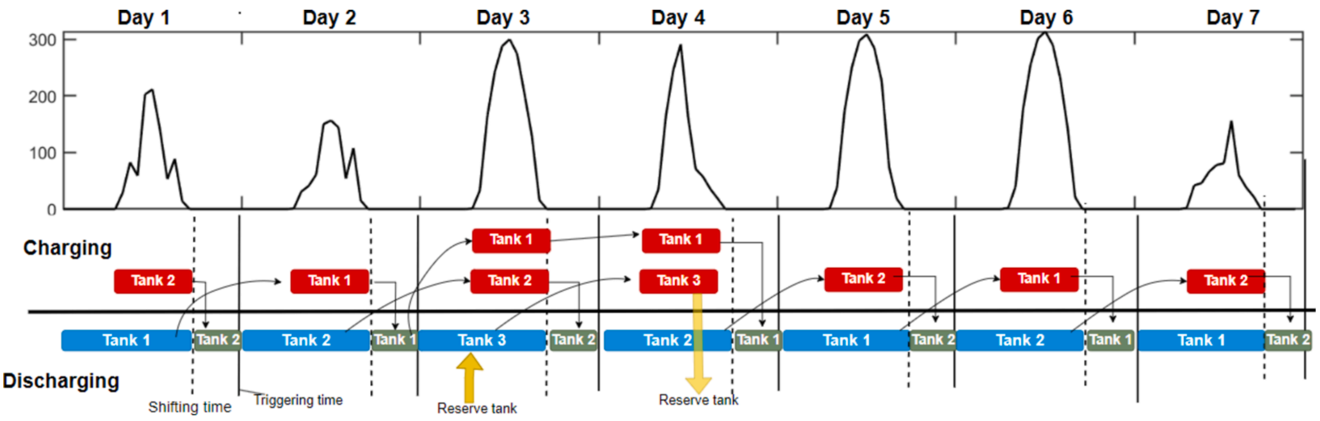

Fig. 13. System operation based on the examined week.

Table 3
Daily status of three tanks.

Day		Tank 1	Tank 2	Tank 3
1	Initial Temperature	40 °C	40 °C	40 °C
	Initial Liquid Fraction	1	0	1
	Mode	*Discharging*	*Charging*	*Idle*
2	Initial Temperature	43.2 °C	51.82 °C	37 °C
	Initial Liquid Fraction	0	1	1
	Mode	*Charging “low mode”*	*Discharging*	*Idle*
3	Initial Temperature	46.24 °C	42 °C	34.31 °C
	Initial Liquid Fraction	0	0	1
	Mode	*Idle*	*Charging*	*Discharging*
4	Initial Temperature	42.08 °C	45.87 °C	39.01 °C
	Initial Liquid Fraction	0	1	0
	Mode	*Charging*	*Discharging*	*Charging*
5	Initial Temperature	50.64 °C	37.55 °C	49.95 °C
	Initial Liquid Fraction	1	0	1
	Mode	*Discharging*	*Charging*	*Idle*
6	Initial Temperature	38.8 °C	41.2 °C	45.43 °C
	Initial Liquid Fraction	0	1	1
	Mode	*Charging*	*Discharging*	*Idle*
7	Initial Temperature	56.47 °C	40.72 °C	41.6 °C
	Initial Liquid Fraction	1	0	1
	Mode	*Discharging*	*Charging*	*Idle*
	Final Temperature	39.39 °C	39.85 °C	38.28 °C
	Final Liquid Fraction	0	1	1

until the evening of the next day when another tank, having been charged, is connected. If the charged tank has undergone a low charging mode—meaning the SAHP has only provided sensible heat to the SAT tank due to low solar irradiance and low buffer tank temperature—it cannot be triggered at midnight. In such instances, a reserve tank is connected to the heating system.

The control strategy illustrated in Fig. 12 outlines the charging and discharging operations of the three tanks, which are further detailed in Fig. 13. The daily status of the three tanks over a one-week operation period is presented in Table 3. This shows that during this period, the low mode is activated once, and the two-tank charging mode is utilized once. It should be noted that at the beginning of the simulation, the temperatures of the three tanks are set to 40 °C, and the liquid fractions of two of them are 1. At the end of the week-long simulation, the liquid fractions of two tanks remain at 1, and the final temperatures are 39.39 °C, 39.85 °C, and 38.28 °C. This slight temperature variation demonstrates that the system nearly returns to its original state. To describe the operations over this one-week period, the subsequent figure is provided, showing temperature variations and system operation modes.

Fig. 14 shows the average temperature variation of three tanks and the hot water delivery temperature to the building, providing insight into system operation and the effectiveness of the control strategy in managing heat storage and solar energy utilization.

At the onset of the simulation, Tank 1 is linked to the building, and the PCM tubes are triggered at midnight. The average temperature of the Tank 1 rises from 40 °C to 57 °C within 1 h due to the absence of heating demand from the building. As evening heat demand arises, the temperature of Tank 1 drops to 45 °C at 7 PM, prompting the connection of Tank 2 to the heating line. On the first day, Tank 2 is charged by the heat pump, reaching a temperature of 68 °C by 1 PM. However, heating continues until the PCMs are fully melted, ending at 7 PM. Upon connection to the heating system, Tank 2 loses sensible heat, causing the temperature to decline to 52 °C, and the PCM tubes are triggered at midnight. The tank then provides heating to the building on the second day.

On the second day, with low solar irradiance and a relatively low buffer tank temperature, the heat pump operates in “low mode,” resulting in Tank 1′s temperature reaching 60 °C with limited latent heating for PCMs. Consequently, Tank 1 is connected to the system at 8 PM, and its temperature decreases to 39.9 °C when it is replaced by Tank 3 (reserve tank) as Tank 1 was not being charged.

On the third day, Tank 3 is triggered, causing its temperature to rise from 34 °C to 57 °C for heating the building. Subsequently, its supply temperature drops to 40 °C at 7 PM and is replaced by Tank 2, which was charged during the day and can provide heat to the building through sensible heat until midnight, after which triggering is activated.

On the fourth day, Tank 2 provides the usual heating during the day, while Tanks 1 and 3 are charged by the heat pump, thanks to sufficient solar irradiance and buffer tank temperature. After triggering, the temperature of Tank 2 increases from 45.8 °C to 57 °C, then drops to around 40 °C by 5 PM, at which point Tanks 2 and 3 both contribute to heating the building. On the fifth and sixth days, the heating operates as usual. On the evening of the sixth day, the building’s heating demand is low, resulting in limited sensible heat loss from Tank 1. Although the triggering does not increase the temperature of Tank 1, the benefit is observed as the latent heat is retained without any supercooling.

Fig. 14d displays the water delivery temperature to the building, obtained from the tank shifting and control strategy of the three tanks. The delivery temperature is slightly higher than the average tank temperatures due to the thermocline in the water tanks. Each day, except for the second day, delivery temperatures increase to around 70 °C as the charged tank is connected to the system in the evening. On the second day, due to the low operation mode, the temperature of the charged tank

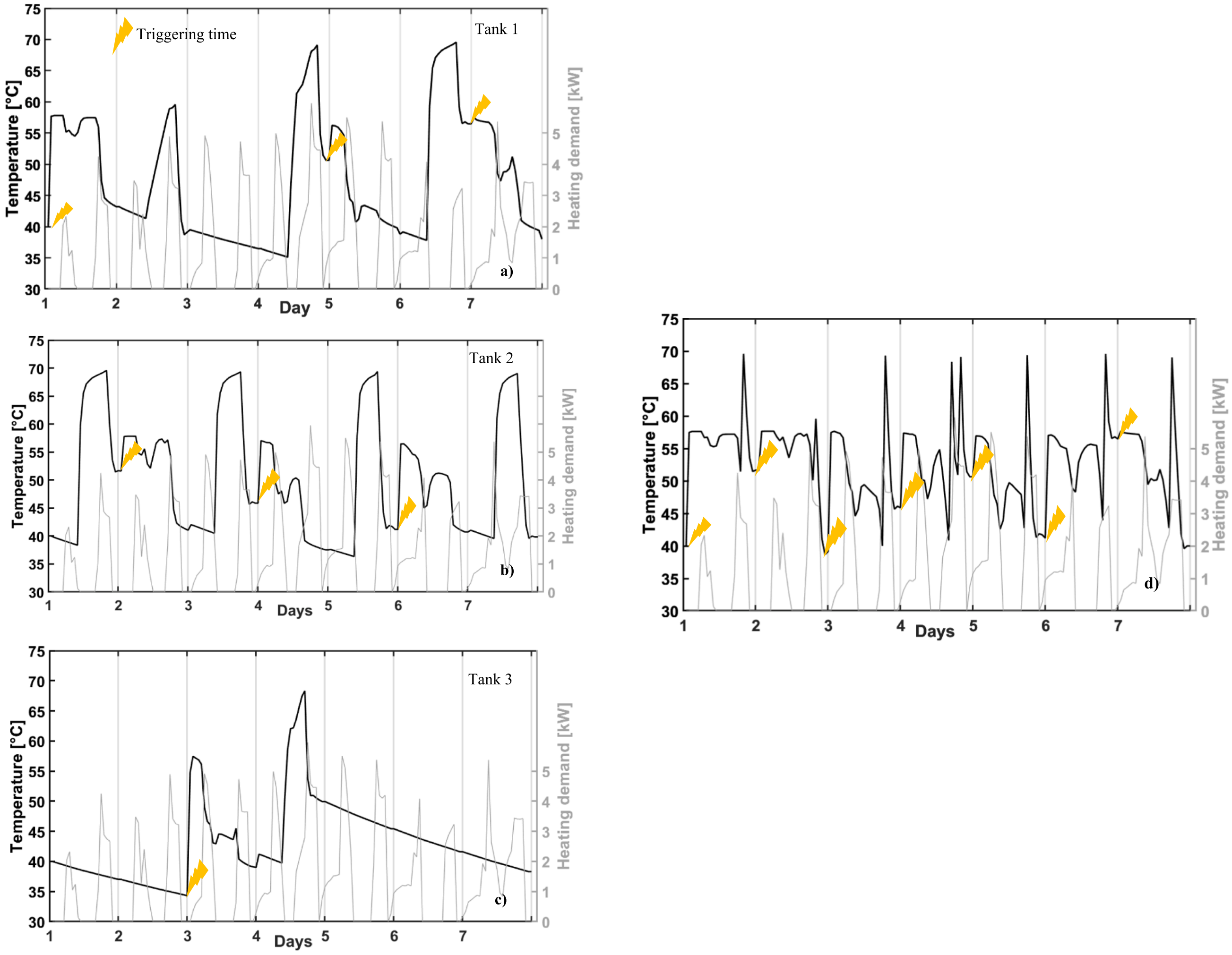

Fig. 14. Water temperature variations of the **a)** Tank 1, **b)** Tank 2, **c)** Tank 3 and **d)** Water delivery temperature to the building.

reaches 60 °C. On the evening of the fourth day, Tank 1 and Tank 3 contribute to heating as they are both charged that day, resulting in a profile with two peaks.

Fig. 15a illustrates the heat pump heating output and building heat demand profiles over the course of the examined week. On weekdays, the heating profile of the house consists of morning and evening peaks, which align with typical residential energy consumption patterns globally. The heat pump heating period begins at 9 AM daily and ends no later than 7 PM, depending on the heating requirements. In the second day's heating profile depicted in Fig. 15a, it is evident that the heat pump adopts "low mode" charging (heating is limited to 1 kW) as directed by the developed control method. Furthermore, on the fourth day, the heat pump provides additional heating, as indicated by the prolonged 7-kW heating period. On this day, two PCM storage tanks are charged, while the subsequent days exhibit a more typical profile as the system operates ideally. Moreover, the variations in the PCM liquid fraction during the charging periods are also shown. During these periods, except on the second day, the PCM liquid fraction increases to 1. On the fourth day, both Tank 1 and Tank 3 are charged simultaneously. Fig. 15b shows the variation in buffer tank temperature and SAHP-SAT compressor consumption profile over a one-week period. The performance of the heat pump and the buffer tank temperature demonstrate a similar trend, as the buffer tank serves as the heat source for the heat pump. Consequently, the COP is primarily dependent on the buffer tank temperature, which, in turn, is influenced by solar availability and the heat extracted by the heat pump.

On the second day, due to weak solar irradiance, the control methodology decided to operate the system in "low mode." As a result, the heat extracted from the buffer tank was minimal, causing its temperature to rise from 16 °C to 26 °C. This increase in temperature would subsequently enhance the heat pump's performance on the following day. Additionally, it is evident from the figure that on the fourth day, the buffer tank temperature decreases from 32 °C to 2 °C, indicating a significant heat extraction due to the utilization of two PCM tanks. As the buffer tank temperature declines, the instantaneous COP decreases from 4.8 to 2.6. However, the buffer tank temperature drops from 20 °C to 14 °C by the end of the seven-day simulation, which suggests that the real system's performance is only slightly lower than the simulation, especially on the last day.

4.3. Performance comparison of the systems

When comparing the performances of the examined three systems, ASHP shows the highest electricity consumption, totalling 107.9 kWh during the week under examination. The SAHP unit which has no PCM, directly heats the building consumes 68 kWh. The PCM-enhanced SAHP-SAT system consumes 80.5 kWh. The results reveal that the use of PCM tanks leads to increased electricity consumption compared to using only the SAHP. This outcome is expected since the SAHP unit provides heating only when required, whereas the SAHP-SAT unit charges the PCM tanks regardless of demand profiles. This charging process involves heat losses through heat exchangers, and the PCM tanks also lose heat

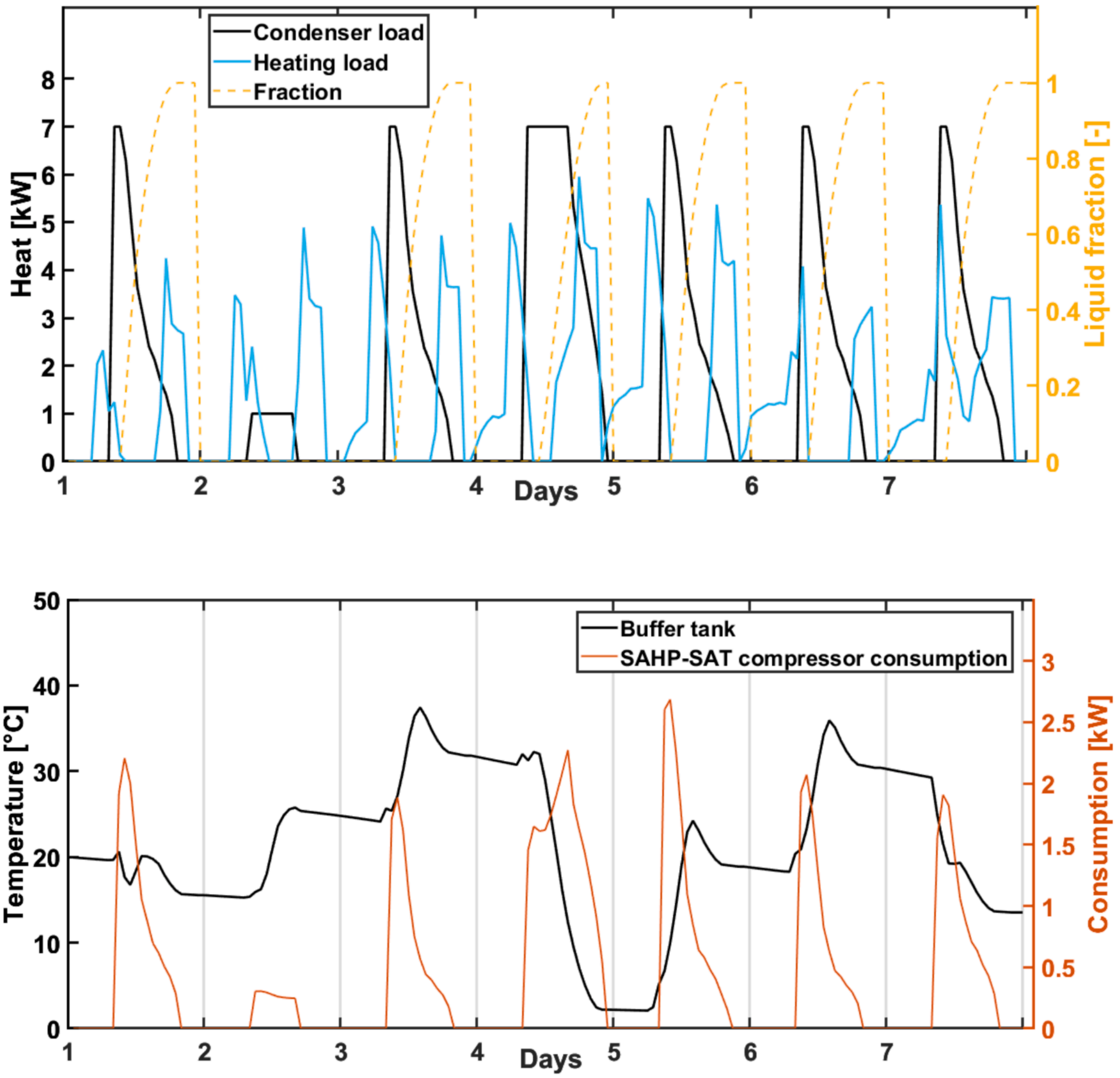

Fig. 15. **(a)** SAHP heating output compared with building heating demand with change of PCM liquid fraction. **(b)** Buffer tank temperature variation and SAHP-SAT compressor consumption.

during their standby conditions. Although the heat loss comprises only sensible heat, it amounts to approximately 6 kWh when the PCM tank temperature decreases from 40 °C to 30 °C. Therefore, this increase in electricity consumption is within expectations for a one-week operational period.

Notably, despite the increased electricity usage, the concept remains effective, as the SAHP provided precisely the heating demand of 245 kWh, resulting in a weekly COP of 3.6. Conversely, the SAHP-SAT unit supplied 287 kWh of heat to charge the PCM storage tanks, resulting in a COP of 3.56. These COP values indicate that while using PCM storage tanks increases the overall heat output, it does not enhance the heat pump’s efficiency, as reflected by the slightly lower COP and increased electricity usage.

However, employing the SAHP-SAT system reduces electricity consumption by 25% compared to conventional ASHP systems. The main contribution of the study lies in demonstrating the potential for load shifting compared to SAHP and ASHP systems. As observed in Fig. 16, the consumption pattern of the SAHP-SAT system typically begins at 9 AM, with the peak consumption occurring mostly around 10 AM.

In order to show the demand shifting in a clear way, Fig. 16 illustrates the total energy consumption profile of the system over the course of a week, aggregated by hour. The data represents the sum of hourly compressor consumption across all seven days, providing insights into the system’s energy usage patterns throughout the week. To calculate the total energy consumption of the system over the course of a week, hourly compressor consumption data was recorded for each day. These hourly consumption values were then summed across all seven days for each hour of the day. For instance, the total consumption at 9 AM on any given day was obtained by summing the compressor consumption at 9 AM from each of the seven days. Similarly, this process was repeated for each hour of the day, resulting in a comprehensive assessment of the system’s energy usage patterns throughout the week.

For the conventional ASHP system, the peak electricity consumption occurs at 6 PM and remains high until 10 PM, with an additional morning peak observed from 6 AM to 9 AM. Similarly, SAHP consumption follows a similar trend but with lower consumption levels. However, these peak hours coincide with domestic grid peak hours, adding further stress to the grid. Given the intensive efforts of governments and societies to transition from boilers to heat pumps in residential areas to reduce carbon emissions, this transition could potentially worsen the grid stress in the future. Therefore, the SAHP-SAT unit evidently shifts electricity demand to the 9 AM-1 PM period,

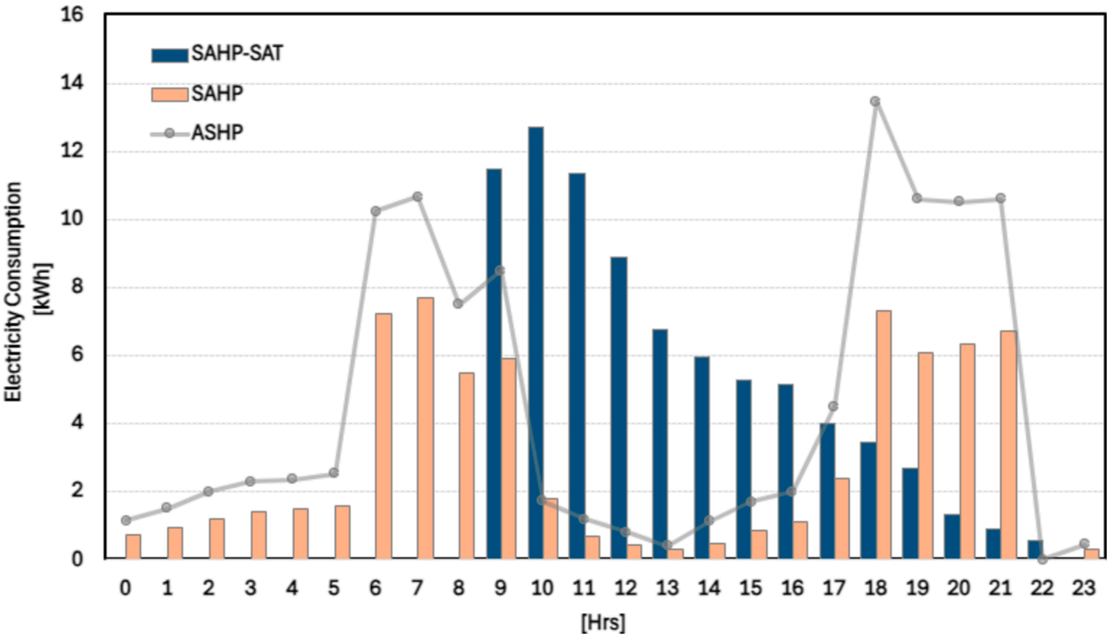

Fig. 16. Total energy consumption profile over a week (05 February to 11 February) given in 24 h.

offering a promising solution for future operations.

5. Conclusions

In this study, a solar-assisted heat pump unit integrated with controllable crystallization of supercooled PCM (SAHP-SAT) has been modelled, and its performance is compared with conventional air source and solar heat pump systems. The concept is demonstrated using three PCM storage tanks, and a control methodology has been developed to ensure smooth operation and effective demand shifting. The developed PCM storage tank model is validated by CFD work in order to find out the charging time. In the comprehensive modelling, the degree of supercooling is also considered for the use of a reserve tank and its stored latent heat to provide sufficient heating to the building. In order to control the system, threshold values for system decision during a week-long operation were chosen as solar irradiance values of 280 W/m^2 and 200 W/m^2 and buffer tank temperatures of 30 °C and 20 °C. These values are used to determine whether to engage in usual charging, charging in "low mode," or charging two tanks together during operation. Based on the numerical investigations, conclusions are drawn as follows.

- *The effect of buffer tank size on SAHP performance is limited. Increasing the buffer tank volume from 600 L to 2000 L results in a performance improvement of only 4.4% when using a 40 m^2 collector area.*
- *To meet the building's heating requirements using PCM tanks, a 358-liter PCM storage tank, including 150 L of water, is charged by the SAHP unit every day. Given that the daily heating demand of the house fluctuates between 20 kWh and 40 kWh, the time for changing tanks varies between 5 PM and 9 PM.*
- *Among the compared systems, the SAHP unit showed the least electricity consumption at 68 kWh, followed by the SAHP-SAT unit at 80.5 kWh, and the less efficient ASHP unit consumed 107.9 kWh. Correspondingly, COP considering the heating demand profile was achieved with SAHP at 3.6, followed by SAHP-SAT at 3, and lastly ASHP at 2.26. It is important to mention that this analysis covers only one week, and control values were set to charge all the tanks used during this period for comparison. Using more PCM storage tanks would provide greater flexibility in arranging the charging schedule on sunny days and allow for more reserve tanks to provide heating.*
- *Although the electricity consumption is higher with the SAHP-SAT system, the unit operates efficiently with a COP of 3.56 when considering the condensation heat. Since the system heats the PCM storage tanks daily, there are heat exchanger losses and ambient heat losses, which require additional heating. However, the conventional SAHP unit directly provides heating to the building without incurring storage losses.*
- *The proposed unit successfully shifts electricity demand from domestic peak hours (6 AM to 9 AM and 5 PM to 8 PM) to off-peak hours. The SAHP consumed a total of 48.5 kWh of electricity during peak hours, which accounts for 71% of the total consumption for the week. In contrast, the SAHP-SAT unit consumed 22.94 kWh of electricity during peak hours, representing 28.5% of the total consumption.*

CRediT authorship contribution statement

Cagri Kutlu: Writing – original draft, Software, Investigation. **Mehmet Tahir Erdinc:** Validation, Software. **Abdullah Dik:** Writing – original draft, Methodology. **Ziwei Chen:** Writing – review & editing. **Qinghua Lyu:** Writing – review & editing. **Yuehong Su:** Writing – review & editing, Supervision, Conceptualization. **Saffa Riffat:** Supervision, Project administration, Investigation, Funding acquisition.

Declaration of competing interest

The authors declare the following financial interests/personal relationships which may be considered as potential competing interests: [Saffa Riffat reports financial support was provided by Engineering and Physical Sciences Research Council. If there are other authors, they declare that they have no known competing financial interests or personal relationships that could have appeared to influence the work reported in this paper].

Acknowledgements

The auhors would like to acknowledge Engineering and Physical Sciences Research Council (EPSRC), Grant No: EP/T02318X/1 for the financial support to this research.M.T. Erdinc acknowledges the support provided by Scientific and Technological Research Council of Turkey BIDEB 2219 with Grant No: 1059B192202957. He also acknowledges the University of Nottingham for hosting.

Appendix 1. Heat pump model

The heat pump unit consists of four main components, compressor, condenser, expansion valve and evaporator.

For heat pump simulation, the given assumptions are considered:

- The condensation and evaporation processes in the condenser and evaporator are assumed to be at constant pressures.
- The subcooling and superheating temperatures are assumed to be 3 °C.
- The evaporation temperature in the heat pump is decided by the buffer tank temperature. An 8 K pinch temperature approach is assumed from the buffer tank and evaporator to ensure appropriate heat transfer.
- The condensation temperature is fixed at 70 °C to properly charge the PCMs.

The phase of the refrigerant is changes from saturated mixture to superheated vapor in the evaporator by absorbing the stored heat in the buffer tank. The temperature and pressure of the refrigerant is calculated by the Eq. (A1) and Eq. (A2). Where T_{eva} is evaporation temperature, $\Delta_{superheating}$ represents temperature difference related to the additional heat absorbed beyond the baseline evaporation temperature. Where, x is quality of the refrigerant, x = 1 indicates that the refrigerant is saturated vapour.

$$T_1 = T_{eva} + \Delta_{superheating} \tag{A1}$$

$$P_1 = \mathrm{f}(T = T_{eva}, x = 1) \tag{A2}$$

the enthalpy h_1 and entropy s_1 are calculated at this initial superheated state using Eq. (A3) and Eq. (A4).

$$h_1 = \mathrm{f}(T = T_1, P = P_1) \tag{A3}$$

$$s_1 = \mathrm{f}(T = T_1, P = P_1) \tag{A4}$$

As the compressor operates, it increases the pressure and temperature of the refrigerant. The h_{2s} is calculated assuming isentropic compression, is calculated using Eq. (A5).

$$h_{2s} = \mathrm{f}(s = s_1, P = P_2) \tag{A5}$$

Using the compressor isentropic efficiency, the actual enthalpy at the compressor outlet (2) can be calculated by Eq. (A6) as follows:

$$h_2 = h_1 + \frac{(h_{2s} - h_1)}{\eta_{comp}} \tag{A6}$$

At the condenser exit properties can be calculated using Eq. (A7) to Eq. (A9). Where T_{con} represents the condensation temperature and $\Delta_{subcooling}$ is the subcooling temperature.

$$T_3 = T_{con} - \Delta_{subcooling} \tag{A7}$$

$$P_3 = \mathrm{f}(T = T_{con}, x = 0) \tag{A8}$$

$$h_3 = \mathrm{f}(T = T_3, P = P_3) \tag{A9}$$

After the condenser, the refrigerant moves through the expansion valve. The pressure decreases at isenthalpic process.

Heating load is calculated by Eq. (A10):

$$\dot{Q}_{con} = \dot{m}_r \times (h_2 - h_3) \tag{A10}$$

Work consumed by the compressor $\dot{W}_{compressor}$ is calculated as follows:

$$\dot{W}_{comp} = \dot{m}_r \times (h_2 - h_1) \tag{A11}$$

Appendix 2. Heat storage tank model

PCM tubes are placed inside the tank and the tank is filled with water which allows continuous heat transfer between the PCM and the water. Convection heat transfer happens between water and PCM outer node. The PCM tube is divided into radial elements (Δr) from centre to edge, thus, conduction heat transfer happens between PCM elements.

Figure A1 shows the PCM tank layout and heat transfer between nodes inside the PCM tank. For each cylindrical PCM tube, heat conduction in both radial (Δr) and longitudinal directions (Δx) were considered. Convection heat transfer occurs between all the PCM tubes and their surrounding water in each element. The water in each element is also exposed to convection heat loss via tank wall and conduction happens between adjacent elements.

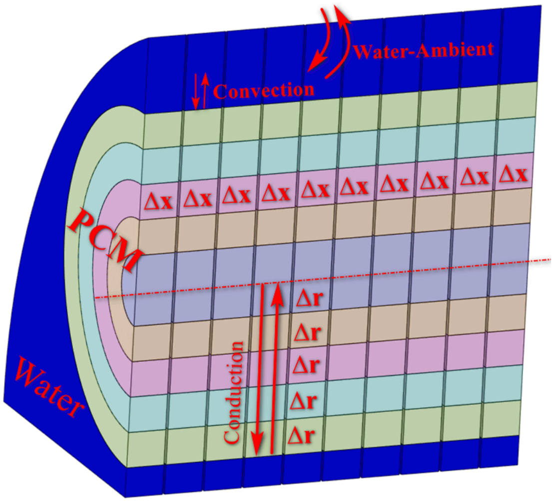

Fig. A1. Discretized heat transfer model

Generalized energy equations of the PCM is adopted from Manfrida et al.[48]:

$$V_{PCMj,n} \bullet \rho_{PCMj,n} \bullet L_{PCMj,n} \bullet \frac{\partial \phi_{j,n}}{\partial t} - V_{PCM_{j,n}} \bullet \rho_{PCM_{j,n}} \bullet c_{p,PCM_{j,n}} \bullet \frac{\partial T_{PCMj,n}}{\partial t} = \dot{Q}_{W_n-PCMj,n} + \dot{Q}_{PCM(j-1),n-PCMj,n} + \dot{Q}_{PCMj,n-PCMj,(n+1)} \tag{A12}$$

j indicates radial nodes (Δr) and n indicates horizontal nodes (Δx). ϕ is PCM liquid fraction, $V_{PCMj,n}$ is volume, $\rho_{PCMj,n}$ is density and $L_{PCMj,n}$ is the heat of fusion per unit mass of the PCM j$^{\text{th}}$ element at horizontal node number n. $\dot{Q}_{W_n-PCMj,n}$ is convection heat transfer rate between water and the PCM element. $\dot{Q}_{PCM(j-1),n-PCMj,n}$ is conduction heat transfer rate between PCM nodes in radial direction and $\dot{Q}_{PCMj,n-PCMj,(n+1)}$ is for conduction heat transfer rate between PCM nodes in horizontal direction. Eq. (A12) covers the outer PCM node in the tube but, for middle PCM nodes, convection heat transfer between water and PCM is replaced with conduction heat transfer with other radial neighbouring PCM nodes.

For the water element, energy balance equation is given in Eq. (A13):

$$T_{w,n}(i+1) = T_{w,n}(i) + \frac{\dot{Q}_{cond,n}(i) + \dot{Q}_{loss,n}(i) + \dot{Q}_{W_n-PCMj,n}(i)}{M_{st,i} \bullet c_{p,w}} \bullet \Delta t \tag{A13}$$

$\dot{Q}_{W_n-PCMj,n}(i)$ is convection heat transfer rate between water and PCM tube outer element in the n$^{\text{th}}$ element, which is given by:

$$\dot{Q}_{W_n-PCMj,n}(i) = h_{wn-PCMj,n} \bullet A_{w-PCMj,n} \bullet \left(T_{w,n} - T_{PCMj,n}\right) \tag{A14}$$

Where $h_{wn-PCMj,n}$ and $A_{w-PCMj,n}$ are convective heat transfer coefficient and heat transfer surface area between PCM and water element, respectively. $T_{w,n}$ and $T_{PCMj,n}$ indicate water and PCM element temperatures, respectively. The convective heat transfer coefficient $h_{wn-PCMj,n}$ is determined using CFD.

To find heat loss to the environment, Eq. (A15) can be used:

$$\dot{Q}_{loss,n}(i) = U_t \bullet A_{tank,n} \bullet \left(T_{container} - T_{w,n}(i)\right) \tag{A15}$$

As the PCM cylinders are in placed in a container which is in underground. $A_{tank,n}$ indicates heat transfer area of the one node in tank. It is a surface area between water and the surrounding air of the container. U_t is overall tank heat loss coefficient.

Data availability

The authors are unable or have chosen not to specify which data has been used.

References

[1] Cabeza LF, et al. CO2 mitigation accounting for Thermal Energy Storage (TES) case studies. *Appl Energy* 2015;155:365–77. https://doi.org/10.1016/j.apenergy.2015.05.121.

[2] Liu X, Zhu J, Wang J, Fu Y, Zhang H, Niu J. Zero fluctuation: Electric-fluctuation-elimination heat pump system with water storage tank based on time-of-use tax. *Energy Build* 2023;279. https://doi.org/10.1016/j.enbuild.2022.112703. 112703.

[3] Tyagi VV, Buddhi D. PCM thermal storage in buildings: A state of art. *Renew Sustain Energy Rev* 2007;11(6):1146–66. https://doi.org/10.1016/j.rser.2005.10.002.

[4] Qiao X, Kong X, Fan M. Phase change material applied in solar heating for buildings: A review. J Energy Storage 2022;55, no. PD. https://doi.org/10.1016/j.est.2022.105826. 105826.

[5] Wang G, et al. Review on sodium acetate trihydrate in flexible thermal energy storages: Properties, challenges and applications. J Energy Storage 2021;40, no. May. https://doi.org/10.1016/j.est.2021.102780. 102780.

[6] Wang Y, Yu K, Peng H, Ling X. Preparation and thermal properties of sodium acetate trihydrate as a novel phase change material for energy storage. *Energy* 2019;167:269–74. https://doi.org/10.1016/j.energy.2018.10.164.

[7] Zhou G, Xiang Y. Experimental investigations on stable supercooling performance of sodium acetate trihydrate PCM for thermal storage. *Sol Energy* 2017;155:1261–72. https://doi.org/10.1016/j.solener.2017.07.073.

[8] Zhang Z, Duan Z, Chen D, Xie Y, Cao X, Wang J. Sodium acetate trihydrate-based composite phase change material with enhanced thermal performance for energy storage. J Energy Storage 2020;34(December 2021). https://doi.org/10.1016/j.est.2020.102186. 102186.

[9] Ma Z, Bao H, Roskilly AP. Study on solidification process of sodium acetate trihydrate for seasonal solar thermal energy storage. *Sol Energy Mater Sol Cells* 2017;172(January):99–107. https://doi.org/10.1016/j.solmat.2017.07.024.

[10] Dannemand M, Englmair G, Kong W, Furbo S. Experimental investigations of multiple heat storage units utilizing supercooling of sodium acetate trihydrate: Stability in application size units. J Energy Storage 2024;86, no. PA. https://doi.org/10.1016/j.est.2024.111194. 111194.

[11] Kutlu C, et al. Incorporation of controllable supercooled phase change material heat storage with a solar assisted heat pump: Testing of crystallization triggering and heating demand-based modelling study. J Energy Storage 2022;55, no. PD. https://doi.org/10.1016/j.est.2022.105744. 105744.

[12] Sakurai K, Yoshinaga N, Yagi R, Tomimatsu N, Sano K. Effect of embedding sodium acetate trihydrate on the Ag anode in an electrical nucleation cell of a supercooled

latent heat storage material. Sol Energy 2018;173(September):1306–14. https://doi.org/10.1016/j.solener.2018.08.014.

[13] Dong C, Qi R, Yu H, Zhang L. Electrically-controlled crystallization of supercooled sodium acetate trihydrate solution. *Energy Build* 2022;260. https://doi.org/10.1016/j.enbuild.2022.111948. 111948.

[14] Dong C, Jia S, Lu F, Wu S, Chen W. Experimental study on the electrically-triggered crystallization behavior of supercooled copper foam-based and expanded graphite-based sodium acetate trihydrate. *Sol Energy Mater Sol Cells* 2024;269, no. January. https://doi.org/10.1016/j.solmat.2024.112766. 112766.

[15] Englmair G, et al. Crystallization by local cooling of supercooled sodium acetate trihydrate composites for long-term heat storage. *Energy Build* 2018;180:159–71. https://doi.org/10.1016/j.enbuild.2018.09.035.

[16] Dannemand M, Schultz JM, Johansen JB, Furbo S. Long term thermal energy storage with stable supercooled sodium acetate trihydrate. *Appl Therm Eng* 2015;91:671–8. https://doi.org/10.1016/j.applthermaleng.2015.08.055.

[17] Englmair G, Moser C, Schranzhofer H, Fan J, Furbo S. A solar combi-system utilizing stable supercooling of sodium acetate trihydrate for heat storage: Numerical performance investigation. *Appl Energy* 2019;242(December 2018):1108–20. https://doi.org/10.1016/j.apenergy.2019.03.125.

[18] Englmair G, Moser C, Furbo S, Dannemand M, Fan J. Design and functionality of a segmented heat-storage prototype utilizing stable supercooling of sodium acetate trihydrate in a solar heating system. Appl. Energy 2018;221:522–34. https://doi.org/10.1016/j.apenergy.2018.03.124.

[19] Kutlu C, Zhang Y, Elmer T, Su Y, Riffat S. A simulation study on performance improvement of solar assisted heat pump hot water system by novel controllable crystallization of supercooled PCMs. *Renew Energy* 2020;152:601–12. https://doi.org/10.1016/j.renene.2020.01.090.

[20] Kutlu C, Zhang Y, Lyu Q, Su Y, Riffat S. Direct-expansion solar-assisted heat pump coupled with crystallisation-controlled supercooled PCM for shifting building electricity demand. *Energy Build* 2023;301, no. October. https://doi.org/10.1016/j.enbuild.2023.113660. 113660.

[21] Zhou G, Li Y, Zhu M. Experimental investigation on space heating performances of supercooled thermal storage units with sodium acetate trihydrate. *Energy Build* 2022;271. https://doi.org/10.1016/j.enbuild.2022.112329. 112329.

[22] Kutlu C, Su Y, Lyu Q, Riffat S. Thermal management of using crystallization-controllable supercooled PCM in space heating applications for different heating profiles in the UK. *Renew Energy* 2023;206(January):848–57. https://doi.org/10.1016/j.renene.2023.02.077.

[23] Chen W, Zhou G. Numerical investigation on thermal performance of a solar greenhouse with synergetic energy release of short- and long-term PCM storage. *Sol Energy* 2024;269, no. January. https://doi.org/10.1016/j.solener.2024.112313. 112313.

[24] Le KX, Huang MJ, Wilson C, Shah NN, Hewitt NJ. Tariff-based load shifting for domestic cascade heat pump with enhanced system energy efficiency and reduced wind power curtailment. *Appl Energy* 2020;257(September 2019). https://doi.org/10.1016/j.apenergy.2019.113976. 113976.

[25] Fischer D, Madani H. On heat pumps in smart grids: A review. *Renew Sustain Energy Rev* 2017;70(November 2016):342–57. https://doi.org/10.1016/j.rser.2016.11.182.

[26] Kelly NJ, Tuohy PG, Hawkes AD. Performance assessment of tariff-based air source heat pump load shifting in a UK detached dwelling featuring phase change-enhanced buffering. *Appl Therm Eng* 2014;71(2):809–20. https://doi.org/10.1016/j.applthermaleng.2013.12.019.

[27] Baeten B, Rogiers F, Helsen L. Reduction of heat pump induced peak electricity use and required generation capacity through thermal energy storage and demand response. *Appl Energy* 2017;195:184–95. https://doi.org/10.1016/j.apenergy.2017.03.055.

[28] Harris B, Walker A. Heat pumps 2023.

[29] Watson SD, Crawley J, Lomas KJ, Buswell RA. Predicting future GB heat pump electricity demand. *Energy Build* 2023;286. https://doi.org/10.1016/j.enbuild.2023.112917. 112917.

[30] Dik A, Kutlu C, Sun H, Calautit JK, Boukhanouf R, Omer S. Towards Sustainable Urban Living: A Holistic Energy Strategy for Electric Vehicle and Heat Pump Adoption in Residential Communities. Sustain. Cities Soc. 2024:105412. https://doi.org/10.1016/j.scs.2024.105412.

[31] Olympios AV, Sapin P, Freeman J, Olkis C, Markides CN. Operational optimisation of an air-source heat pump system with thermal energy storage for domestic applications. *Energy Convers Manag* 2022;273, no. August. https://doi.org/10.1016/j.enconman.2022.116426. 116426.

[32] Dik A, Kutlu C, Omer S, Boukhanouf R, Su Y, Riffat S. An approach for energy management of renewable energy sources using electric vehicles and heat pumps in an integrated electricity grid system. *Energy Build* 2023;294, no. May. https://doi.org/10.1016/j.enbuild.2023.113261. 113261.

[33] "How much of the UK's energy is renewable?," 2024. https://www.nationalgrid.com/stories/energy-explained/how-much-uks-energy-renewable (accessed Apr. 17, 2024).

[34] Jangsten M, Kensby J, Dalenbäck JO, Trüschel A. Survey of radiator temperatures in buildings supplied by district heating. *Energy* 2017;137:292–301. https://doi.org/10.1016/j.energy.2017.07.017.

[35] "IESVE,2020." https://www.iesve.com/software/virtual-environment (accessed Sep. 04, 2021).

[36] Cruickshank CA, Harrison SJ. Heat loss characteristics for a typical solar domestic hot water storage. *Energy Build* 2010;42(10):1703–10. https://doi.org/10.1016/j.enbuild.2010.04.013.

[37] Freeman J, Guarracino I, Kalogirou SA, Markides CN. A small-scale solar organic Rankine cycle combined heat and power system with integrated thermal energy storage. *Appl Therm Eng* 2017;127:1543–54. https://doi.org/10.1016/j.applthermaleng.2017.07.163.

[38] Duffie JA, Beckman WA. *Solar Engineering of Thermal Processes*. John Wiley; 2013.

[39] Kutlu C, Li J, Su Y, Pei G, Riffat S. Off-design performance modelling of a solar organic Rankine cycle integrated with pressurized hot water storage unit for community level application. *Energy Convers Manag* 2018;166(15):132–45. https://doi.org/10.1016/j.enconman.2018.04.024.

[40] Hundy GF. Refrigeration, Air Conditioning and Heat Pumps. 5th ed. Butterworth-Heinemann; 2016.

[41] Roccatello E, Prada A, Baggio P, Baratieri M. Impact of startup and defrosting on the modeling of hybrid systems in building energy simulations. *J Build Eng* 2023;65(August 2022). https://doi.org/10.1016/j.jobe.2022.105767. 105767.

[42] Xu T, Chiu JN, Palm B, Sawalha S. Experimental investigation on cylindrically macro-encapsulated latent heat storage for space heating applications. *Energy Convers Manag* 2019;182(November 2018):166–77. https://doi.org/10.1016/j.enconman.2018.12.056.

[43] Taborek J. Longitudinal flow in tube bundles with grid baffles. *AIChE Symp Ser* 1989;85(269):72–8. https://doi.org/10.1615/hedhme.a.000258.

[44] Ghahramani Zarajabad O, Ahmadi R. Numerical investigation of different PCM volume on cold thermal energy storage system. J Energy Storage 2018;17(February):515–24. https://doi.org/10.1016/j.est.2018.04.013.

[45] Mahdi MS, Mahood HB, Mahdi JM, Khadom AA, Campbell AN. Improved PCM melting in a thermal energy storage system of double-pipe helical-coil tube. *Energy Convers Manag* 2020;203(November 2019). https://doi.org/10.1016/j.enconman.2019.112238. 112238.

[46] S.A. Klein, "Engineering equation solver academic professional 2020: V10.951. F-Chart Software (2020).".

[47] B. Geological Survey, "Temperature and Thermal Properties (Basic)," 2011. [Online]. Available: http://www.metoffice.gov.uk.

[48] Manfrida G, Secchi R, Stańczyk K. Modelling and simulation of phase change material latent heat storages applied to a solar-powered Organic Rankine Cycle. *Appl Energy* 2016;179:378–88. https://doi.org/10.1016/j.apenergy.2016.06.135.